

Dynamical Invigoration of Electrified Storms

Dipjyoti MUDIAR¹, Earle R. Williams², Sunil D Pawar¹, Anupam Hazra¹, Rama Krishna Karumuri³, V. Gopalakrishnana⁴, Mahen Konwar¹, Rakesh Ghosh¹, Manoj A Domkawale¹, Kaustav Chakravarty¹, Manoj K Srivastava⁵, and Bhupendra Nath Goswami⁶

¹Indian Institute of Tropical Meteorology

²Massachusetts Institute of Technology

³King Abdullah University of Science and Technology

⁴Indian Institute of Tropical Meteorology

⁵Banaras Hindu University

⁶Cotton University

November 26, 2022

Abstract

The recent emergence of compelling evidence (Mudiar et al., 2018, 2021a 2021b) regarding a significant impact of cloud electrification on rain microphysical processes raises curiosity on the potential dynamical implications of cloud electrification. In this study, the consequence of cloud electrification has been explored from a perspective of interaction between cloud microphysics and dynamics using observational data and numerical models in a tropical condition. It is shown that the strongly electrified (SE) clouds exhibit a reduced value of rain intercept parameter, N_0 relative to the weakly electrified (WE) counterpart facilitated by the in-cloud electric field. This process results in a reduction in rain evaporation rate in the warm phase of the cloud, thereby enhancing the surface rain intensity. From a dynamical perspective, the reduced rain evaporation rate gives positive feedback to storm energetics by reducing latent cooling. The reduced latent cooling delays the downdraft thereby facilitating an invigoration of convection. This electrically induced invigoration is termed ‘Dynamical Invigoration of Electrified Storms’.

Dynamical Invigoration of Electrified Storms

Dipjyoti Mudiar¹, Earle Williams², S. D. Pawar¹, Anupam Hazra¹, Rama Krishna Karumuri³, V. Gopalakrishnana¹, Mahen Konwar¹, Rakesh Ghosh¹, Manoj A Domkawale¹, Kaustav Chakravarty¹, M. K. Srivastava⁴, and B N Goswami⁵

¹Indian Institute of Tropical Meteorology, Ministry of Earth Sciences, Pune, India, 411008

²Massachusetts Institute of Technology, Cambridge, MA USA

³King Abdullah University of Science and Technology, Thuwal, Saudi Arabia

⁴Banaras Hindu University, Varanasi, India 221005

⁵Cotton University, Guwahati, India 781001

Abstract

The recent emergence of compelling evidence (*Mudiar et al.*, 2018, 2021a 2021b) regarding a significant impact of cloud electrification on rain microphysical processes raises curiosity on the potential dynamical implications of cloud electrification. In this study, the consequence of cloud electrification has been explored from a perspective of interaction between cloud microphysics and dynamics using observational data and numerical models in a tropical condition. It is shown that the strongly electrified (SE) clouds exhibit a reduced value of rain intercept parameter, N_0 relative to the weakly electrified (WE) counterpart facilitated by the in-cloud electric field. This process results in a reduction in rain evaporation rate in the warm phase of the cloud, thereby enhancing the surface rain intensity. From a dynamical perspective, the reduced rain evaporation rate gives positive feedback to storm energetics by reducing latent cooling. The reduced latent cooling delays the downdraft thereby facilitating an invigoration of convection. This electrically induced invigoration is termed ‘*Dynamical Invigoration of Electrified Storms*’.

31

32

33

34 **1. Introduction**

35

36 Clouds are manifestations of uplift of air either by convection, orography or by waves in the
37 atmosphere. Convective overturning enables the atmosphere to release the stored potential
38 energy by converting it to the kinetic energy of air motion. The cloud droplets resulting from the
39 convection transformed into raindrops by different microphysical processes and produce surface
40 precipitation as the end product which drives the Earth's hydrological cycle. The microphysical
41 processes that convert the cloud droplets to raindrops differ depending upon the type and stages
42 of convection (active and decaying). For example, in convective precipitation with a stronger
43 updraft, precipitation arises from the collection of cloud droplets in the warm phase of the cloud
44 and by freezing, riming and aggregation of snow in the mixed-phase in the presence of
45 substantial supercooled liquid water (*Houze, 1997*). When the updraft weakens in the decaying
46 stage of a storm, the growth of precipitation particles primarily happens through vapor diffusion
47 and aggregation in the mixed-phase region of the cloud (*Houze, 1997*), which is known as
48 stratiform precipitation. Once the precipitation particles form, they evolve through different
49 microphysical processes such as collision, coalescence, breakup, evaporation and sublimation.
50 The prevailing microphysical processes determine the raindrop size distribution, RDSD
51 (*Konwar et al., 2014*) and hence the total amount of rain received at the surface (*Morrison et al.,*
52 *2009, 2012*). Hence a proper understanding of the cloud microphysics that impact the rain
53 amount and intensity is very important.

54 One factor that is external to the convection, but can feedback on the convection
55 and hence on the rain amount and its intensity is the aerosol size and its number concentration.
56 Numerous high impact investigations can be found in the literature in support of this scenario
57 (*Rosenfeld, 1999; Tao et al., 2012; Khain et al., 2005; Rosenfeld, 2008* and reference therein).
58 The other factor (also external to convection) that could potentially impact the rain formation
59 mechanisms is cloud electrification (*Pruppacher and Klett, 1996* and references therein). Cloud

60 electrification and consequent lightning is the visual manifestation of the interaction between
61 cloud convection and hydrometeors. The lightning-producing clouds exhibit vertical electric
62 fields reaching 400 kVm^{-1} (Winn et al., 1974) with hydrometeor charge up to $\pm 250 \text{ pC}$ (*Christian*
63 *et al.*, 1980). Hence, this fraction of clouds can be termed as strongly electrified (SE). In
64 lightning-producing clouds, different charging mechanisms involving ice phase microphysical
65 processes mediated by stronger vertical air velocity produces the required electric field for
66 electrical breakdown. The primary charging mechanism is the non-inductive charging where
67 collision between smaller ice crystals and larger size graupels is considered as the primary
68 process (*Takahasi*, 1978; *Bruning et al.*, 2007; *Bruning et al.*, 2010).

69 Although the common initiator of both precipitation and lightning is cloud convection, both
70 show different sensitivity to the convective intensity (*Williams*, 2005). While lightning remains
71 associated with deeper and stronger updraft than does precipitation, numerous observations
72 reported that both these observables remain well correlated during tropical thunderstorms
73 (*Piegrass et al.* 1983, *Mudiar et al.*, 2021a, *Choudhury et al.*, 2021). One potential explanation
74 of this observed correlation is the substantial contribution of precipitation to storm electrification
75 and consequent lightning production (*Williams and Lhermitte*, 1983). They reported that the
76 gravitational energy associated with falling precipitation could substantially contribute to the
77 electrical energy of a lightning discharge. However, not much attention has been paid to
78 understanding the reverse feedback process, i.e., the impact of electrification on precipitation
79 formation despite having extensive evidence for the same both from laboratory and numerical
80 studies (see *Pruppacher and Klett*, 1996). Recent observational studies have shown that rain
81 microphysical processes in strongly electrified (SE) clouds are distinctly different from those in
82 weakly electrified (WE) clouds, which is conventionally attributed to the vigorous ice factory in
83 SE clouds (*Mattos et al.*, 2016). Weakly electrified clouds (exhibiting weaker updraft intensity)
84 are often warm clouds that do not strongly penetrate the freezing level. The SE cloud produces a
85 larger number of bigger raindrops relative to the WE counterpart. The presence of larger
86 raindrops in SE clouds can be attributed to three characteristic microphysical processes as
87 discussed below.

88 (a) Melting of larger graupel/hail particles

89 This is the conventional hypothesis to explain the presence of larger raindrops in lightning-
90 producing clouds (SE). The coexistence of a larger concentration of smaller ice particles and
91 bigger graupels along with supercooled raindrops in the mixed-phase region of cloud are
92 considered essential for charge separation and consequent electrification (*Takahashi, 1978;*
93 *Mattos et al., 2016*). Numerous dual-pol radar observations indicate large radar reflectivity
94 ($Z > 30$ dBZ) in the mixed-phase region, indicating the presence of larger graupel/hail particles
95 and aggregates (*Mattos et al., 2016, Carey and Rutledge, 2000*). The more vigorous the storm ice
96 factory, the stronger will be the electrification. When these particles drift downward, they
97 produce bigger raindrops below the melting layer upon melting. However, while drifting down
98 below the melting level, the raindrop evolves through collision, coalescence, breakup and
99 evaporation (readers are referred to *Konwar et al., 2014* and *Raut et al., 2021* for a detailed
100 description on the vertical evolution of drops size).

101 **(b) Electric fields induce coalescence of raindrops below the melting layer**

102 The in-cloud electric field and surface charge can also enhance the collision-coalescence
103 growth of raindrops (*Mudiar et al., 2021b* and references therein). In the presence of stronger
104 electrical environments typical of lightning-producing clouds, the enhanced collision-
105 coalescence of raindrops facilitated by cloud electric field (*Pruppacher and Klett, 1996* and
106 references therein) below the melting layer can broaden the RSD towards the larger drop
107 sizes (*Mudiar et al., 2018*). It has been observed that in a SE cloud, the electrically induced
108 coalescence of raindrops increases the number concentration of bigger raindrops, thereby
109 reducing the number of smaller drops (*Mudiar et al., 2021b*).

110 **(c) Lightning-induced precipitation formation**

111 Thunderstorms are known to exhibit a close association between lightning rate and
112 rainfall rate (*Piepgrass et al., 1982; Price and Federmesser 2006, Mudiar et al., 2021a*). The pre-
113 discharge updraft levitation of precipitation particles is known to occur in the so-called balance
114 level situated at 6-7km MSL height (*Lhermitte and Williams, 1985*). It may be noted here that
115 the pre-discharge levitation of precipitation particles may be either kind: aerodynamic levitation
116 or electrical levitation. Lightning reduces the pre-discharge electric force. The reduction of
117 electrical forces after the lightning allows the precipitation particles to drift downward in the

118 form of graupel and small hail. The melting of these particles produces numerous large as well as
119 small drops below the melting layer, thereby enhancing the surface rainfall known as rainingush.
120 This rainingush may occur from the collapse of aerodynamic as well as electrical levitation of
121 particles. A recent study by Mudiar et al., (2021a) suggests that lightning can modify the size of
122 raindrops by depositing ions near the channel. The attachment of these ions to the raindrops
123 make them electrified. The electrified drops coalesce efficiently to produce larger raindrops and
124 thereby enhance the rain rate. For a detailed explanation of this process, readers are referred to
125 Mudiar et al. (2021a).

126 The simulation of precipitation using Numerical Weather Prediction (NWP) models has been
127 improved significantly at synoptic and mesoscales over the years (Boer et al., 2014). However,
128 large mean absolute errors (MAE~10 to 14) for the heavy rain intensity (>10mm) still persist in
129 the quantitative precipitation forecast (QPF)(*Giannaros et al.*, 2015). One potential source of this
130 large MAE may be inaccurate information on the RDS. An accurate information on the RDS
131 is considered important for understanding precipitation physics and improving the microphysics
132 parameterization in NWP models (*Steiner et al.*, 2004). On the other hand, it has been reported
133 that a substantial amount of the rainfall (~57%) in the latitude belt of 30° N–30° S could be
134 attributed to Mesoscale Convective Systems (MCS) (*Virts and Houze*, 2015). The convective and
135 the stratiform regimes of MCS over the Maritime Continent remain associated with strong
136 electrification (*Williams et al.*, 2010). This suggests that a large fraction of tropical precipitation
137 comes from strongly electrified clouds where electrical forces can affect the rain microphysical
138 processes (Sun et al., 2018). So, an effective parameterization of the electrical effect in the
139 physics schemes of weather/climate models can provide a potential opportunity to improve the
140 representation of this fraction of cloud in the NWP models. Also, many studies suggest that the
141 prevailing microphysical processes can strongly impact the in-cloud dynamics (e.g. updrafts and
142 downdrafts) (*Grabowski*, 2015; *Rosenfeld*, 2008; *Morrison et al.*, 2009; *Hazra et al.*, 2013).
143 However, how the feedback between the anomalous dynamics and microphysics influences the
144 resultant precipitation is not known. As the electrical impact on the rain microphysical processes
145 is now reasonably well established (*Mudiar et al.*, 2018, 2021a, 2021b, 2022), feedback to the
146 dynamical features of storms from the electrically modified microphysical processes can be
147 expected in a SE tropical cloud systems.

148 With this background, in this paper we investigate a NWP model's sensitivity to electrically
149 modified RDS parameters and a possible feedback mechanism of cloud electrification to the
150 dynamical parameters of storms. First, the clouds are electrically distinguished based on
151 observational data sets. The microphysical properties of both types of cloud are investigated and
152 some statistics have been derived for the RDS parameters in SE rain events. The second half of
153 the paper is dedicated to a numerical experiment using a numerical weather model. Results from
154 the simulation experiment have been presented in order to investigate the sensitivity of model-
155 simulated cloud microphysical and dynamics parameters to electrically-modified RDSs. In the
156 discussion section, some possible mechanisms of storm invigoration have been discussed. The
157 main conclusions of the paper have been summarized in the conclusion section.

158

159 **2. Data and Methodology**

160 The results and interpretations presented in this paper pertain to analysis of both
161 observational data sets and numerical modeling. Some of the meteorological observations
162 presented here were carried out at the High Altitude Cloud Physics Laboratory (HACPL),
163 Mahabaleshwar, (India; 17.92 N, 73.66 E). The electrical parameters of storms, such as surface-
164 electric field were measured at the Atmospheric Electricity Observatory (AEO) at Pune, (India;
165 18.53N, 73.80E). The distance of the AEO from the HACPL is around 100 km (see Figure 1a).
166 The topographical features and climatology of both the observation sites have been extensively
167 discussed in *Mudiar et al.* (2021a). The measurements of the RDS parameters reported in this
168 study are carried out with a surface-based Joss-Waldvogel disdrometer (JWD) located at the
169 HACPL and a laser optical Particle Size and Velocity (PARSIVEL) disdrometer, located at the
170 AEO. The Doppler spectra obtained from a microrain radar (MRR) installed at the HACPL have
171 been used to study the vertical profiles of radar reflectivity and RDS. There are numerous
172 papers describing the usefulness and limitations of these three measuring instruments (*Joss and*
173 *Waldvogel, 1967; Peters et al., 2005; Löffler-Mang and Joss, 2000; Konwar et al., 2014; Mudiar et*
174 *al., 2018, 2021a*). Hence, with a view to brevity, we will abstain from discussing them again
175 here. However, when necessary the data curation from the instruments and the related
176 measurements errors will be discussed.

177 All the simulation experiments reported in the current study are performed using the
178 Advanced Weather Research and Forecasting (WRF-ARW) model version 3.9.1. The WRF
179 model is developed by the National Center for Atmospheric Research (NCAR). It is a fully
180 compressible, non-hydrostatic, terrain-following 3D mesoscale model. Two kinds of simulation
181 experiments are carried out: a set of idealized simulations and a set of observed case simulations.
182 The model set up and model initialization for the idealized simulations are extensively discussed
183 in section 3.5. The simulations for the observed cases are carried out considering four nested
184 domain (d01, d02, d03, d04) configurations. The four domains are configured with a horizontal
185 grid spacing of 27km, 9km, 3km and 1km, respectively. Figure 1b depicts the geographical
186 coverage of the model domain. The domain d04 (innermost) is centered on the HACPL. For the
187 observed case simulations, the initial and boundary conditions are provided from 6 hourly final
188 operational global analysis (NCEP-FNL) data. The NCEP-FNL data is available with $1^\circ \times 1^\circ$
189 horizontal resolution. For long wave radiation, the Rapid Radiative Transfer Model (RRTM) has
190 been used, as discussed in *Mlawer et al. (1997)*. For short wave radiation, the Dudhia scheme
191 (*Dudhia, 1989*) has been used. While the two innermost cloud-resolving domains (3rd and 4th)
192 are treated with explicit convection, the Betts Miller Janjic (BMJ) cumulus parameterization
193 scheme is employed only in the outer two domains (d01 & d02). A microphysical scheme
194 namely the WRF single moment 6 class (wsm6) (*Hong and Lim, 2006*) is used for all the
195 observed case simulations for reasons to be discussed in section 5. The model output from the
196 observed case simulation is compared with the available observed meteorological parameters for
197 validation. The daily rainfall information over the area considered for this study is obtained from
198 TRMM-3B42 datasets and surface measurements from the Indian Meteorological Department
199 (IMD).

200 As the main objective of this paper is to evaluate the microphysical processes and their
201 possible dynamical feedback in electrically distinguished rainfall events, the accurate electrical
202 characterizations of the events is important. The electrical distinguishability of clouds can be
203 ascertained in two ways: either through measurement of the surface electric field below the storm
204 or by ensuring the presence/absence of lightning near the observatories. The presence of
205 lightning in the vicinity of the observatory ensures a stronger electrical environment inside the
206 cloud. For the rain events observed at the HACPL, the electrical distinguishability of the events
207 is ascertained by observing the lightning activity near the HACPL with the Maharashtra

208 Lightning Location Network (MLLN) as there is no measurement of the surface electric field
209 available at the observatory. The measurement of the surface electric field during storms
210 observed at the AEO was carried out with an electric field mill. The field mill was kept in a pit
211 with its sensor flush with the ground. Interested readers are referred to *Mudiar et al. (2021a)* for
212 the detailed measuring techniques of lightning and electric field. For the SE storms which are
213 considered for simulation, some of the available cloud properties and meteorological features
214 derived from the surface-based JW disdrometer and the Moderate Resolution Imaging
215 Spectroradiometer (MODIS) (Terra platform) collection 6 (Baum et al., 2012) are documented in
216 Table 1 along with the observed lightning flash rates from the MLLN.

217 3. Results

218 As extensive evidence regarding the electrical modification of raindrop size has already been
219 reported in *Mudiar et al. (2018, 2021a, 2021b, 2022)*, so here we will only focus on the
220 implication of the presence of larger raindrops in the SE cloud. First, we will select two
221 electrically distinguished rain events (one SE and one WE) and characterize them
222 microphysically. Figure 2a and 2b depict the Height Time Index (HTI) of the radar reflectivity
223 factor, Z for two rainfall events observed over the HACPL on 13 May 2015 and 4 October 2014,
224 derived from the MRR. Both the events exhibit the initial convective and subsequent stratiform
225 rainfall regimes. The stratiform regime is characterized by a prominent radar bright band at a
226 MSL height of 4.3 km. The event shown in Figure 2a is characterized by the presence of
227 lightning activity near the HACPL (see Figure 3), while for event 2b, no lightning activity was
228 recorded by the MLLN in the neighborhood of the HACPL. Hence the event shown in Figure 2a
229 is considered SE category and the event in Figure 2b is WE category. The lightning-producing
230 storms observed in the pre- and post-monsoon season over the Indian subcontinent include air
231 mass thunderstorms and squall lines. The time evolution of lightning on 13 May 2015 in the
232 vicinity of the HACPL suggests that this SE storm is an air mass thunderstorm and is stationary
233 in nature (see Figure S1 in supporting information). The corresponding rain rates are shown in
234 Figure 2(c-d). While the convective regimes are characterized by heavy rain rate ($>10 \text{ mm hr}^{-1}$),
235 the stratiform regimes exhibit a lower rain rate ($<10 \text{ mm hr}^{-1}$) consistent with the observation of
236 Tokay and Short, (1996). The transition regime from convective to stratiform which is
237 characterized by lower rainfall rate is evident in both events. The time evolution of the Mass-

238 weighted Diameter (MWD) of raindrops measured by the JWD depicted in Figure 2(e-f) shows
239 the presence of significantly larger raindrops in the SE event compared to the WE event. This is
240 consistent with many polarimetric radar observations of lightning-producing storms (Kumjian
241 and Ryzhkov, 2008; Mattos et al., 2016). This is expected as explained above. The most
242 contrasting feature between the SE and WE events can be seen in the time evolution of the rain
243 intercept parameter (N_0) as shown in Figure 2(g-h). While the WE event exhibits a high
244 frequency fluctuation in the time evolution of N_0 , the SE event shows a relatively stable
245 evolution of N_0 with a lower magnitude as well. The observed larger value of N_0 in the transition
246 regime in both events is found to be consistent with Zhang et al., (2017). This distinction in N_0
247 is further explored in the section below from the microphysical perspective.

248 **3.3 The characteristics of the rain intercept parameter N_0 in SE events**

249 The values of N_0 depend primarily on the rain type and intensity (Zhang et al., 2008). A study
250 over the HACPL by Konwar et al. (2014) also revealed that vertical variations of N_0 are distinct
251 for the convective and stratiform regimes of clouds. It has been commonly observed that the
252 value of N_0 increases with the rain liquid water content, W (Zhang et al., 2008, Morrison et al.,
253 2012). At higher W , a larger number of raindrops formed by collision-coalescence of droplets
254 produce a higher rain number concentration, thereby increasing the value of N_0 . Figure 4(a)
255 shows the scatter plot representation of N_0 as a function of W for 33 SE events observed over the
256 HACPL. These two parameters are calculated from the corresponding RDSM measured by the
257 disdrometer located at the HACPL following the method of moments as in Konwar et al. (2014).
258 From this Figure, it can be seen that N_0 exhibits a decreasing trend with increasing values of W ,
259 albeit large scatter across W . It may be noted that because of the large variability in N_0 , the trend
260 looks weaker. A separate trend analysis between $\log(N_0)$ and W for the SE event reported in
261 Figure 2a depicts a correlation coefficient, $r=-0.64$ indicating a significant trend between the two
262 variables. See also Figure S2 in the supporting information A. This is in contrast to the
263 observations of Zhang et al. (2008) and Morrison et al. (2012), but consistent with the
264 observation of Tokay and Short (1996) who observed that the value of N_0 exhibits a decreasing
265 trend with rainfall rate. The two events reported in Figure 2 have been superimposed in Figure
266 4(a). The similar characteristics of the event shown in Figure 4a (red dots), imply that this event
267 can be treated as a representative sample of SE events. On the other hand, the event shown in the

268 right panel of Figure 2b (black square), exhibits the same characteristics as reported by *Zhang et*
269 *al.* (2008) and *Morrison et al.* (2012).

270 The values of N_0 averaged over the entire rainy periods of all 33 SE events are shown in
271 the bar graph representation in Figure 4(b). It can be seen that N_0 exhibits large variability
272 among the events considered. This is consistent with the previous observation which shows that
273 values of N_0 depend on the rain type and the intensity of convection (Zhang et al., 2017). For
274 purposes of comparison, in the same Figure, we have overlaid the values of N_0 for 17 rain events
275 for which no lightning was observed in a box of 100 km \times 100 km. The absence of lightning
276 indicates that these events may not be as strongly electrified as lightning-producing events. It can
277 be seen that these WE events exhibit higher values of N_0 (mean= 68389 m⁻³mm⁻¹) compared to
278 the SE (N_{0_mean} =1649 m⁻³mm⁻¹) events. This implies that SE rain events exhibit a lesser
279 concentration of smaller raindrops than the WE counterpart. The SE electrified storms achieve
280 this microphysical characteristic by virtue of enhanced collision-coalescence of raindrops below
281 the melting layer. Numerous laboratory and numerical investigations have revealed that in the
282 presence of an ambient electric field, raindrops collide more frequently relative to an electrically
283 neutral condition by virtue of the electrical attraction (Schlamp et al.,1976; Pruppacher and Klett,
284 1996; Khain et al, 2004). It is also a known fact that two electrified colliding drops coalesce
285 more easily than their neutral counterpart (Ochs and Czys 1987; Freier,1960). In the case of
286 collision between electrified raindrops, the electrostatic attraction between the colliding
287 raindrops enhances the drainage of the air film trapped between the drops which help the drops
288 to coalesce permanently (Ochs and Czys, 1987). The efficient coalescence of smaller raindrops
289 in the presence of an electric field resulted in a substantial reduction in the number concentration
290 of smaller raindrops (Mudiar et al.,2021b) and hence the value of N_0 .

291 As evident from the discussion above, two possible hypotheses can be considered to explain
292 this distinct characteristic of N_0 in SE rain events, viz, the ice factory hypothesis and the
293 electrically induced coalescence of raindrops below the melting layer. The melting of ice phase
294 hydrometeors (for example graupel and hail), which invariably remain associated with SE
295 clouds, will produce raindrops through three different processes

296 (1) Direct melting of graupel and hail.

297 This process results in large drops below the melting layer. While these large raindrops
298 drift downward to the surface, they face collisional breakup, thereby producing numerous
299 tiny raindrops in the warm phase of the storm along with the large raindrops (Friedrich et
300 al. 2013; Raut et al., 2021). Also, during the convective regimes of a storm, a large
301 amount of liquid water can be transported to the mixed-phase region of the storms by a
302 stronger updraft, where ice crystals grow by the riming process. These rimed ice crystals
303 result in an increase in the value of N_0 upon melting below the melting layer (Bringi et
304 al., 2002).

305 (2) Shedding of raindrops from the surface of melting particles.

306 While melting, hail/graupel particles (diameter >19 mm) shed smaller drops in the
307 diameter range from 0.5mm to 2.0 mm, with a modal diameter of 1 mm (Lesins et al.,
308 1980, Rasmussen et al. 1984, Pruppacher and Klett, 1996, Ryzhkov et al., 2013). The
309 shedding of drops from the surface of melting particles can produce 1000-2000 smaller
310 drops (1mm) per kilometer below the melting layer (Pruppacher and Klett, 1996). This
311 will result in an increase in the number concentration of smaller raindrops and hence in
312 the value of N_0 .

313 (3) Spontaneous break up of large raindrops.

314 This raindrop breakup process under the influence of aerodynamic forces will again result
315 in numerous smaller raindrops (Low and List, 1982a), thereby contributing positively to
316 N_0 .

317 Clear evidence of dominant raindrop breakup can be seen for the WE event in Figures 2f
318 and 2h with a high-frequency fluctuation in the raindrop size and the values of N_0 . On the
319 other hand, electrically induced coalescence of drops below the melting layer systematically
320 reduces the number of smaller raindrops, thereby effectively reducing the value of N_0 (see
321 Figure 3f in Mudiar et al., 2021b). Evidently, we shall consider the electrically-induced
322 coalescence of millimeter-sized raindrops as a dominant mechanism for reduction in the
323 value of N_0 in the SE rain events relative to the WE ones, albeit the inherent uncertainty from
324 the melting process. An important microphysical implication of this observation is that WE
325 events will exhibit a larger rain evaporation rate than the SE events as explained in *Morrison*
326 *et al.* (2009). This aspect has been explored further in the next section.

327 3.4 The effect of electrification on the rain evaporation rate

328 Rain evaporation is a major sink of the latent heat released by the condensation of water
329 vapor. The available latent heat also transforms to kinetic energy of updraft. If the vapor density
330 at the surface of cloud/raindrops exceeds the vapor density of the ambient environment,
331 evaporation of the drops takes place as vapor is diffused away from the drops. It is known that
332 smaller drops evaporate faster than larger drops because the rate of change of drop size through
333 evaporation is inversely proportional to the drop radius (*Pruppacher and Klett, 1996*). As
334 explained above, the SE cloud exhibits fewer smaller raindrops relative to the WE counterpart.
335 One major anticipated implication of this distinct RDS in both types of cloud may be the
336 change in rain evaporation rate below the melting layer. A significant impact of the rain intercept
337 parameter N_0 on the rain evaporation rate is well known (*Morrison et al., 2009*). The rate of
338 evaporation may be calculated from the RDS parameter using the following equation (*Reisner*
339 *et al., 1998*)

$$340 \left(\frac{\partial q_r}{\partial t}\right)_{EVAP} = \frac{2\pi N_{0r}(S-1)}{A'+B'} \left\{ \frac{0.78}{\lambda^2} + 0.31 \left(\frac{a_r \rho}{\mu}\right)^{1/2} \frac{\Gamma(b_r/2+5/2)}{\lambda^{b_r/2+5/2}} \right\} \quad (1)$$

341 Here, q_r is the rain mixing ratio (kg kg^{-1}), N_{0r} (m^{-4}) is the RDS intercept parameter, S is the
342 saturation ratio of liquid water, A' and B' are the thermodynamic parameters associated with the
343 release of latent heat, λ (m^{-1}) is the slope parameter of the RDS, a_r and b_r are the parameters
344 related to the fall speed of the rain (fall speed for a given diameter D can be expressed as $a_r D^{b_r}$
345), μ ($\text{kg m}^{-3} \text{s}^{-1}$) is the dynamic viscosity of air, ρ is the air density (kg m^{-3}) and Γ is the gamma
346 function. This equation is similar to the ones appearing in *Rutledge and Hobbs (1983)* and
347 *Morrison et al. (2009)*.

348 Figure 5 depicts the rain evaporation rate (ER) below the melting layer calculated by
349 using equation (1) for both the SE and WE events reported in Figure 2. The evaporation rate is
350 calculated from the MRR-derived RDS averaged over the entire stratiform regimes.
351 Considering the large attenuation of the MRR signal in the heavy rainfall regimes (see *Konwar et*
352 *al., 2014, Mudiar et al., 2018*), the convective parts of the events ($R > 10 \text{ mm hr}^{-1}$) are avoided in
353 the analysis of rain evaporation rate. This analysis with the MRR is limited to the domain below
354 the MSL height of 4 km to avoid the presence of ice phase hydrometeors, as Figure 2 shows the

355 presence of the melting layer at 4.6 km MSL height. A significant reduction in the evaporation
356 rate is observed below 3.6 km MSL height for the SE event. This is expected because the SE
357 events depict the presence of more number of larger raindrops and a lesser concentration of
358 smaller drops below the melting layer than the WE events, as shown in *Mudiar et al.* (2018).
359 Although the convective regimes ($R > 10 \text{ mm hr}^{-1}$) are avoided for ER analysis considering a
360 significant attenuation of MRR signal in larger rainfall rates (*Peters et al.*, 2005), a qualitative
361 analysis can be made. *Kessler* (1974) has parameterized the rain evaporation rate as $ER \propto N_0^{0.35}$.
362 Since the convective regimes are known to produce a larger value of N_0 (*Waldvogel*, 1974,
363 *Tokay and Short*, 1996, *Zhang et al.*, 2017) relative to the stratiform counterpart, it follows that
364 the convective regimes will exhibit a larger magnitude of ER depending upon the ambient
365 relative humidity (see equation 1). For the events reported in Figure 2, the respective mean
366 values N_0 for the convective regimes of the SE and WE events are observed to be 4975 and
367 10718 in the units of $\text{m}^{-3} \text{ mm}^{-1}$. Hence, a larger magnitude of rain evaporation rate may be
368 expected for the WE event depending upon the ambient relative humidity.

369 Recent observation shows that surface-measured electric field and raindrop size remain
370 positively correlated. The greater the electric field, the larger will be the raindrops (*Mudiar et al.*,
371 2021b). As there were no electric field measurements for the events shown in Figure 2 at the
372 HACPL, we could not analyze the effect of the electric field on the rain evaporation rate for
373 those events. However, simultaneous measurements of surface electric field and RDSD were
374 available for some of the storms observed over the AEO, in Pune. A few such storms were
375 observed over the AEO on 3 June, 31 August, 8 Sept. and 9 Sept. 2008. While the electric field
376 was measured with an electric field mill (*Pawar et al.*, 2017), the RDSD was measured with an
377 optical disdrometer. The magnitude of surface measured electric field for the events considered
378 varies from 0-5000 V m^{-1} with an observed peak lightning rate of 22 flashes per minute during
379 the mature stage of one of the storms (the storm in Figure 6a). The electric field traces for these
380 storms are shown in Figure S3 in the supporting information along with the peak lightning rates.
381 Figure 6(a-d) depicts the bar graph representation of the N_0 values as a function of the electric
382 field. The time resolution of the disdrometer measurement was 10 seconds. The measured values
383 of N_0 are grouped in bins of electric field of width 500 V m^{-1} for all events. The bars on the
384 graphs represent the mean values of the bins. As expected, at larger magnitudes of E field, N_0
385 exhibits lower values for each of the storms considered. This indicates that at a larger magnitude

386 of electric field, the number of smaller raindrops is reduced substantially in the RDSD spectrum.
387 This can be attributed to the increased coalescence of the smaller drops to form bigger ones as
388 explained in *Mudiar et al.* (2021b). It is may be noted here that the event in Figure 6a exhibited a
389 much larger lightning rate (22 fl. min⁻¹) compared to the rest of the events (3 fl. min⁻¹) and hence
390 a more vigorous ice factory. Also, this event exhibited a lower value of N_0 relative to the rest of
391 the events. For this storm, N_0 exhibits an increasing trend with the lightning rate (see Figure S4
392 in the supporting information) which is expected considering a more vigorous ice factory at a
393 larger lightning rate. The plausible reason for the smaller value of N_0 for this storm relative to the
394 rest of the storms may be a much larger magnitude of the E field ($E_{\max}= 5000 \text{ Vm}^{-1}$) relative to
395 the other events shown in Figure 6b-d ($E_{\max}= 1800 \text{ Vm}^{-1}$).

396 A reduction in smaller raindrop numbers strongly indicates a reduction in the rain
397 evaporation rate as well. The corresponding bar plot of rain evaporation rate as a function of E
398 field (Figure 6e-h) clearly indicates that rain evaporation rate (ER) decreases at the larger
399 magnitude of the electric field. The reduction of rain evaporation rate at a larger magnitude of
400 electric field can be attributed to two physical processes

401 (a) The electrically enhanced coalescence of raindrops substantially reduces the number
402 concentration of smaller raindrops below the melting layer. The larger the magnitude of
403 the electric field, the lesser the number concentration of smaller drops (resulting in
404 smaller value of N_0) as can be seen from Figure 6. This results in a reduction in ER as
405 smaller drops tend to evaporate faster.

406 (b) It has been shown that the electrical attraction between the charged raindrops and the
407 molecular dipoles of water vapor oriented along the electric field (produced by the
408 charged raindrops) may create a water concentration gradient close to the raindrops
409 (*Nielsen et al*, 2011). This charge-dipole interaction may result in a reduction in ambient
410 saturation vapor pressure over electrified raindrops thereby protecting the drops from
411 evaporation. However, a quantitative estimation of this process for millimeter-sized
412 raindrops has yet to be achieved.

413

414 The analysis presented in this section clearly indicates that the raindrop evaporation rate
415 is significantly lowered by the electrification of cloud. This microphysical modification might
416 have important consequences for the cloud dynamics and rain formation. A net evaporation
417 depletes the rain water content, thereby affecting the quantitative precipitation estimation (QPE)
418 (*Kumjian and Ryzhkov, 2010*). A WRF simulation study by *Morrison et al. (2009)* shows that
419 reduced rain evaporation enhances the rainfall amount in the trailing stratiform region of an
420 idealized squall line. They also mentioned that the reduced evaporation rate leads to a reduction
421 in latent cooling in the convective regime, thereby increasing the mean convective updraft
422 intensity. The negative buoyancy produced by evaporative cooling can influence the storm
423 evolution by producing enhanced downdraft (*Srivastava, 1985, 1987*).

424 As the reduction in the values of N_0 in SE events reduces the rain evaporation rate, it is
425 important to investigate the possible feedback it can give to the cloud processes. The cloud-
426 resolving models (CRM) are widely used tools to study cloud processes. To evaluate the
427 microphysical and dynamical implications of a reduced N_0 and consequent evaporation rate in
428 the SE rain events, we have performed some numerical experiments using the WRF model. Two
429 sets of experiments are performed: an idealized 2D simulation and two 3D observed case
430 simulations. The chosen observed SE events for the simulation study are the one shown in Figure
431 2a (13 May 2015) and another one observed at the HACPL on 5 May 2015. The results of the
432 numerical simulation will be presented next.

433 **3.5 Results from Numerical Simulation Experiments**

434 **A. Idealized simulation**

435 As mentioned in section 2, for the numerical experiment, we have used the WRF model
436 which has been extensively used to study cloud processes. *Morrison et al. (2009)* investigated
437 the effect of the rain evaporation rate on the microphysics and dynamics of an idealized storm
438 with WRF 2D squall-line simulations. In the WRF model, the cloud and precipitation size
439 distribution are represented by a gamma distribution

$$440 \quad N(D) = N_0 D^\mu e^{-\lambda D} \quad (2)$$

441 Where N_0 , λ , μ represents the intercept, slope and shape parameters of the RSD, respectively.
442 D indicates the diameter of the particles.

443 Considering $\mu=0$ for rain following *Morrison et al.* (2008), the size distribution of rain can be
444 expressed as an exponential function

$$445 \quad N(D) = N_0 e^{-\lambda D} \quad (3)$$

446 This is commonly known as Marshall-Palmer distribution of raindrops.

447 The one moments (1M) scheme implemented in the WRF model predicts the mass mixing ratio
448 (q) of five hydrometeor species, including cloud droplets, cloud ice, snow, rain, and graupel. A
449 value of N_0 is specified in the physics scheme. The number of hydrometers species, N and λ can
450 be derived from the predicted q and specified N_0 using equations (4) and (5).

$$451 \quad \lambda = \left(\frac{\pi \rho_r N}{q \rho} \right)^{1/4} \quad (4)$$

$$452 \quad N_0 = N \lambda \quad (5)$$

453 Where ρ_r is the density of raindrops (1000 kg m^{-3}) and ρ is the air density (kg m^{-3}).

454 As the purpose of this study is to evaluate model sensitivity to electrically modified N_0 , we
455 have decided to use the one moment scheme where we can specify the value of the observed N_0
456 in the model physics. For our study, we use the WRF single moment six class scheme (wsm6) as
457 explained in *Hong and Lim* (2006). In this scheme, the default value of N_0 is specified as $8 \times$
458 10^6 m^{-4} . This value is widely used for the representation of warm rain (Kessler, 1969).

459 Following *Morrison et al.* (2009), we choose a single 2D domain for the idealized
460 simulation. The grid in both x and y directions is 99 points with a grid spacing of 11m. The
461 model has been initialized using the default input-sounding provided with the WRF for 2D squall
462 line simulations. All the physics options are turned off except for the microphysics (from wsm6).
463 As the initialization is performed with an idealized input sounding, the simulated outputs are not
464 compared with the observations. This experiment serves to produce a simplified interpretation of
465 the results in the absence of the other physics scheme such as radiation physics, cumulus physics
466 and planetary boundary layer physics. Two experiments are carried out: one with the default

467 value of N_0 ($= 8 \times 10^6 m^{-4}$), the other one with a new value of N_0 ($= 1.6 \times 10^6 m^{-4}$). This
468 value is the mean of all the SE events shown in Figure 4(b). The statistics of N_0 for these SE
469 events are depicted in a box plot representation in Figure S5 in the supporting materials.

470 As explained by *Morrison et al.* (2009), a reduction in the value of N_0 should enhance the
471 rain rate at the surface. In Figure 7(a), we have compared the accumulated rain from the two
472 experiments. The default scheme is designated 'wsm6', while the modified run (with N_0
473 $= 1.6 \times 10^6 m^{-4}$) is designated 'wsm6(M)'. As can be seen, 'wsm6(M)' produces a substantially
474 larger amount of rain compared to 'wsm6', although the rain is delayed by 3 hours in wsm6(M).
475 The factor which can potentially enhance the rain rate is the reduced rain evaporation as
476 explained by *Morrison et al.* (2009). As expected, the wsm6(M) exhibits a reduced rain
477 evaporation rate relative to the wsm6 as can be seen from Figure 7(b). But can this much
478 reduction in evaporation rate increase the rain amount so high or are other mechanisms also
479 contributing? What are the consequences of this reduced evaporation rate on storm dynamics?

480 *Morrison et al.* (2009) stated that the evaporation rate can influence the intensity of the
481 convective updraft. They explained that a lower value of N_0 produces a lower evaporation rate
482 which leads to the reduction in latent cooling, thereby increasing the mean convective updraft
483 intensity. Rain evaporation is a major sink of the latent heat released by condensation and vapor
484 deposition. *Tao and Li* (2016) suggested that the more the rain, the stronger will be latent heat
485 release or we can argue conversely: the stronger the latent heat release, the greater the rainfall.
486 An enhanced latent heat release can induce a stronger updraft. To investigate the effect of
487 reduced N_0 in wsm6(M), we have plotted the simulated maximum vertical velocity (W_{max}) in
488 Figure 7(c). It has been observed that wsm6(M) produces substantially larger updraft velocity
489 relative to wsm6, especially in the middle and upper troposphere. One possible cause of this may
490 be the release of more latent heat (indicated by higher rain amount) to induce stronger convective
491 intensity. However, it is important to consider the fact that a change in buoyancy by latent
492 heating may get balanced approximately by condensate loading (see *Grabowski and Morrison,*
493 2020). The other possible cause is the reduction in rain evaporation rate, a consequence of lower
494 N_0 (Snook and Xue, 2008; *Morrison et al.*, 2009). This may happen primarily below the melting
495 layers of the SE cloud. An updraft intensity of such magnitude ($10\text{-}25 m s^{-1}$) is typical of
496 lightning-producing clouds (*Williams*, 2001). It has also been observed that while wsm6

497 produces maximum vertical velocity in the 2nd hour of model integration, wsm6(M) produces
498 maximum vertical velocity in the 4th hour of model integration. This indicates a feedback to
499 cloud vertical velocity from the microphysics in wsm6(M). The idealized simulation experiment
500 shows that a change in the value of N_0 may have important implications for simulated rain
501 accumulation and updraft intensity.

502

503 **B. Simulation of observed SE event**

504 As the idealized simulation experiment incorporating values of N_0 , characteristic of SE
505 events shows a larger rain amount, we are curious to see the effect of N_0 modification in an
506 observed SE event. For that, we have chosen the same SE event shown in Figure 2(a) for the
507 simulation. Some of the meteorological and electrical features for this storm have been
508 documented in Table 1. This storm exhibited a maximum rain rate of 22 mm hr^{-1} with a lightning
509 rate of $4 \text{ flashes min}^{-1}$. Two experiments have been performed: one with the default value of N_0
510 ($= 8 \times 10^6 \text{ m}^{-4}$), and the other one with a new value of N_0 ($= 1.6 \times 10^6 \text{ m}^{-4}$) obtained from
511 observations of SE storms. Figure 8(a) depicts the rain rates from both the simulations averaged
512 over a $25\text{km} \times 25\text{km}$ box centered at the HACPL. As before, the default scheme is indicated as
513 ‘wsm6’, while the modified run is designated as ‘wsm6(M)’. A significantly larger rain rate is
514 observed in wsm6(M) relative to wsm6. This selection of the $25\text{km} \times 25\text{km}$ box is made based on
515 the fact that a larger domain may contain different cloud systems: some are SE and some are
516 WE. As we have perturbed the model physics with a value of N_0 averaged over only the SE
517 events, the inclusion of any probable WE events in the process of spatial averaging may bring
518 inconsistency to the interpretation of the simulated fields. For a comparison, the JWD measured
519 rain intensity at the HACPL is overlaid along with the simulated rain intensities. It may be noted
520 here that, the maximum rain rate observed at the HACPL, may not be a correct representation of
521 the maximum rain rate observed during the storm. A better comparison of accumulated rain rate
522 from observation and simulations has been depicted in Figure 8(b). In this Figure, the
523 accumulated rain averaged over the box from both the simulation experiments have been
524 compared with the observed rain accumulation obtained from Indian Meteorological Department
525 (IMD) and Tropical Rain Measuring Mission (TRMM) 3B-42 precipitation datasets. Some
526 improvement in the accumulated rain is also observed with wsm6(M). The idealized simulation

527 suggests that this improvement may be due to the reduced rain evaporation rate in wsm6(M).
528 This increase in rain rate by virtue of reduced rate of rain evaporation is found to be consistent
529 with the modeling study of *Tao and Li* (2016). A persisting problem in simulating the observed
530 frequency distribution of tropical rainfall by most of the weather/climate models is that the
531 models tend to highly overestimate the frequency of very light rain, and substantially
532 underestimate the frequency of heavy rainfall events (*Goswami and Goswami*, 2016). This study
533 indicates that a proper prediction of the rain intercept parameter, N_0 in models may improve the
534 frequency distribution of heavier precipitation.

535 The results from the idealized simulations as well as the observed case simulations presented
536 above show that an appropriate modification of the rain intercept parameter N_0 (characteristics of
537 SE) can enhance the intensity and the amount of simulated rainfall. The primary cause of this can
538 be attributed to the reduction in rain evaporation rate introduced in the model by the applied
539 modification. However, as mentioned before, a reduction in rain evaporation rate will also
540 increase the net latent heating in the warm phase of the cloud. This may give positive feedback to
541 the cloud updraft by delaying the evaporative-driven downdraft. This argument is consistent with
542 the profile of maximum vertical velocity obtained from the idealized simulation where it is
543 shown that wsm6(M) produces significantly higher vertical velocity in the mid and upper
544 troposphere. From the observed case simulation, we have tried to investigate the storm temporal
545 evolution from a height time index (HTI) plot of area-averaged (25km×25m box) vertical
546 velocity produced by wsm6 and wsm6(M) as shown in Figure 9(a-b). At the beginning of the
547 storm (cumulus stage, 11.30-13.30 IST), larger vertical velocity can be seen in the lower
548 troposphere from both simulations as expected. A common observation of the SE storm suggests
549 the presence of a stronger updraft (9-10 ms^{-1}) in the cumulus phase (*Roger and Yau*, 1989). At
550 15.30 IST, both simulations show the presence of the strongest updraft from 4.5 km to 9.5 km.
551 The presence of the 0° C level at 4.5 km indicates that this region of strongest updraft is in the
552 mixed-phase region of the cloud. The presence of a stronger updraft in the mixed-phase cloud is
553 considered essential for charge separation through the non-inductive charging mechanism
554 (*Takahashi*, 1978). However, the contrasting difference between the two simulations is the
555 expanded updraft core in wsm6(M) in the mixed-phase region. This can be explained by
556 considering the reduced rain evaporation rate (*Morrison et al.*, 2009). This reduction increases
557 the updraft intensity in wsm6(M), as evident from Figure 9(b) relative to 9(a). Please note that

558 while wsm6 produces downdraft at the lower altitudes from the 2nd hour of the simulated storm
559 (13:30 IST), wsm6(M) delays the onset of downdraft to the 5th hour (16:30 IST). This is a direct
560 consequence of reduced latent cooling in wsm6(M). At the later stage of the storm, a weaker
561 updraft prevails in the upper troposphere (Figure 9), while the stronger downdraft can be
562 observed at the lower level, possibly induced by the melting of ice phase hydrometeors (*Houze,*
563 1997). To establish the robustness of the proposed hypothesis, we have carried out a simulation
564 of another SE event (5 May 2015) observed over the HACPL with the same model set up. The
565 accumulated rain (averaged over the 25km×25m box) for both the observed case simulations are
566 documented in Table 1. The modified simulation shows a 76% increase in rain accumulation.
567 Figure 10(a-b) depicts the HTI plot of area-averaged (25km×25m box) vertical velocity produced
568 by wsm6 and wsm6(M), respectively. This Figure also shows that simulation with ‘wsm6(M)’
569 delays the initiation of downdraft relative to the simulation with ‘wsm6’, consistent with the
570 hypothesis of updraft enhancement by reduced rain evaporation rate as in Figure 9(a-b). These
571 findings are consistent with the results from an idealized squall line simulation of *Morrison et*
572 *al.*, (2009). The domain averaged mass mixing ratio of ice phase hydrometeors
573 (ice+graupel+snow) exhibits approximately 26% increase with wsm6(M) relative to wsm6,
574 consistent with the increased updraft intensity (see Table 1). The results from these simulation
575 studies add confidence to our conclusion that a reduction in rain evaporation rate in SE rain
576 events (a consequence of the electrically modified value of N_0) suppresses/delays the downdraft,
577 thereby invigorating the convection.

578 **4. Discussions**

579 Precipitation and cloud electrification, while both are the product of convective instability in
580 the atmosphere, both exhibit different sensitivity to the convective intensity (*Williams, 2005*).
581 However, both can feedback on each other through different microphysical and dynamical
582 processes. The role of precipitation on cloud electrification has been extensively discussed by
583 *Williams and Lhermitte (1983)*. They suggest that falling precipitation could substantially
584 contribute to storm electrification. However, the effect of cloud electrification on precipitation
585 microphysics has only been addressed recently. In a series of paper, *Mudiar et al. (2018, 2021a,*
586 *2021b)* have shown that the cloud electric field could indeed substantially enhance the growth of
587 raindrops. As shown here, because of the electrical enlargement of raindrops, the rain intercept

588 parameter N_0 is reduced considerably in clouds that are associated with a stronger in-cloud
589 electric field, such as lightning-producing clouds. The reduction of N_0 consequently reduces the
590 rain evaporation rate, thereby further enhancing the convective intensity of storms. An analytical
591 discussion of storm invigoration as a consequence of reduced rain evaporation rate has been
592 presented below.

593 Conditional instability, the thermodynamic basis for thunderstorm formation, is driven
594 primarily by Convective Available Potential Energy (CAPE). However, the generation of
595 thunderstorms may also occur in low CAPE conditions depending upon orography and
596 prevailing meteorological conditions (*Murugavel et al.*, 2014). The CAPE can be defined as the
597 accumulated buoyant energy from the level of free convection (LFC) to the equilibrium level
598 (EL) (*Williams and Renno*, 1993)

$$599 \quad CAPE = \int_{LFC}^{EL} R_d (T_{vp} - T_{ve}) d \ln p \quad (6)$$

600 The parcel and environmental virtual temperature are T_{vp} and T_{ve} respectively, R_d is the gas
601 constant of dry air and p is the pressure. A reasonable correlation between CAPE and the total
602 number of lightning flashes is well recognized (*Pawar et al.*, 2012), as the interplay among
603 CAPE, vertical updraft and cloud microphysics dominantly influence the cloud electrical activity
604 and lightning (*Williams*, 2001). Larger CAPE values produce conditional instability in the
605 atmosphere, thereby facilitating vigorous convection with active mixed-phase microphysics and
606 larger lightning activity (*Williams et al.*, 1992). *Emanuel et al.* (1994) suggest that the virtual
607 temperature remains associated with the boundary-layer entropy. They also suggest that the
608 convective downdraft acts to reduce the boundary-layer entropy. The reduced rain evaporation
609 rate in wsm6(M) will essentially reduce the latent cooling and thereby delays the downdraft at
610 the lower level at the earlier stage of the storm, as evident from Figures 9(b) and 10(b). An
611 inhibition in a convective downdraft in wsm6(M) will essentially result in larger boundary-layer
612 entropy. *Williams and Renno* (1993) reported that boundary layer entropy and CAPE remain well
613 correlated in the tropical atmosphere.

614 Also, when the precipitation particles fall to the sub cloud layer, the evaporation
615 contributes to the negative thermal buoyancy. As wsm6(M) is associated with a lower value of
616 N_0 than wsm6, hence the previous scheme should produce a lower evaporation rate as the storm

617 evolves. The lower rain evaporation rate delays the downdraft by reducing the latent cooling,
618 thereby increasing the convective intensity (see *Morrison et al.*, 2009). As this storm
619 invigoration comes from a reduced rain evaporation rate, a consequence of electrical
620 enhancement of raindrops size accompanied by a reduction in the number of smaller drops, we
621 are encouraged to term this positive feedback between microphysics and dynamics of the storm
622 as ‘*Dynamical Invigoration of Electrified Storms*’. The proposed hypothesis has been
623 schematically represented in Figure 11. A potential implication of these results can be discussed
624 from the perspective of tornadogenesis. It has been reported that RDS with larger raindrops
625 (smaller N_0) favors tornadogenesis by weakening the cold pool through reduced evaporation
626 (*Snook and Xue*, 2008). It is known that the initiation of a tornado in a supercell storm is
627 preceded by vigorous lightning (*MacGorman and Burgess*, 1994). The electrification of the
628 storm may act to reduce the rain evaporation rate, thereby assisting in tornadogenesis. However,
629 this needs further investigation as no convincing observational evidence of this process has been
630 reported yet.

631

632 5. Conclusion

633 The investigation of the hypothesis for the influence of cloud electrification on the dynamics
634 of tropical clouds using observational datasets and numerical experiments has resulted in the
635 following conclusions:

- 636 1. Initiated by convective instability, SE clouds with high lightning propensity are
637 associated with larger concentration of bigger raindrop and lesser concentration of
638 smaller raindrop and hence a reduced value of the RDS intercepts parameter N_0 relative
639 to the WE clouds.
- 640 2. The depletion of N_0 results in a reduction of rain evaporation rate in clouds associated
641 with a stronger electrical environment.
- 642 3. The reduction in rain evaporation rate suppresses/delays the downdraft, thereby further
643 invigorating the convection.
- 644 4. The findings here strongly suggest that the representation of the lightning-producing and
645 non-lightning-producing clouds in weather/climate models should be distinct.

646

647 **Acknowledgments:**

648 IITM is funded by the Ministry of Earth Sciences, Government of India. We thank the Director,
649 IITM for his support and encouragement. BNG thanks the Science and Engineering Board
650 (SERB), Government of India, for the SERB Distinguished Fellowship and a research grant. We
651 sincerely thank the scientific and support staff working at the HACPL. The authors thank the
652 following data sources for making the data available: NCEP global final analysis data
653 (<http://dss.ucar.edu/datasets/ds083.2/>), TRMM data products from STORM-PPS
654 (<https://storm.pps.eosdis.nasa.gov/storm/>), and Indian met department gridded rainfall products.

655 **Open Research**

656 The observational data used to prepare the manuscript can be found in the link
657 <https://osf.io/MWCAV/>.

658

659 **References:**

660

661 Baum, B. A., W. P. Menzel, R. A. Frey, D. Tobin, R. E. Holz, S. A. Ackerman, A. K. Heidinger,
662 and P. Yang (2012) MODIS cloud top property refinements for Collection 6, *J. Appl.*
663 *Meteorol. Climatol.*, 51, 1145–1163.

664

665 Bhalwankar, R.V., Sathe, A.B. and Kamra, A.K (2004). The evaporation of the charged and
666 uncharged water drops suspended in a wind tunnel. *J Earth Syst. Sci.* **113**, 129–138
667 <https://doi.org/10.1007/BF02709783>.

668 Boers N, Bookhagen B, Barbosa H, Marwan N, Kurths J and Marengo J (2014). Prediction of
669 extreme floods in the Eastern Central Andes based on a complex networks approach. *Nat*
670 *Commun* 5:5199. doi: 10.1038/ncomms6199

671 Bringi, V. N., Chandrasekar, V., Hubbert, J., Gorgucci, E., Randeu, W. L., & Schoenhuber, M.
672 (2003). Raindrop Size Distribution in Different Climatic Regimes from Disdrometer and
673 Dual-Polarized Radar Analysis, *Journal of the Atmospheric Sciences*, 60(2), 354-365

674 Bruning, E.C., Rust, W.D., Schuur, T.J., MacGorman, D.R., Krehbiel, P.R. and Rison, W.,
675 (2007). Electrical and polarimetric radar observations of a multicell storm in TELEX. *Mon.*
676 *Weather Rev.* 135, 2525–2544. <http://dx.doi.org/10.1175/MWR3421.1>.

677 Bruning, E.C., Rust, W.D., MacGorman, D.R., Biggerstaff, M.I. and Schuur, T.J.(2010).
678 Formation of charge structures in a supercell. *Mon. Weather Rev.* 138, 3740–3761.

679 Carey, L. and S. Rutledge(2000). “The Relationship between Precipitation and Lightning in
680 Tropical Island Convection: A C-Band Polarimetric Radar Study.” *Monthly Weather*
681 *Review* 128 : 2687-2710.

682 Choudhury B.A., B.N. Goswami, Yasmin Zahan, P.V. Rajesh,(2021). Seasonality in power law
683 scaling of convective and stratiform rainfall with lightning intensity over Indian Monsoon
684 regions, *Atmospheric Research*, 248,105265, ISSN 0169-8095.

685 Christian H., C. R. Holmes, J. W. Bullock, W. Gaskell, A. J. Illingworth, and J. Latham (1980).
686 Airborne and ground-based studies of thunderstorms in the vicinity of Langmuir Laboratory,
687 *Q. J. R. Meteorol. Soc.*, 106, 159-174.

688 Dee, D. P., Uppala, S. M., Simmons, A. J., Berrisford, P., Poli, P., Kobayashi, S., et al. (2011) The
689 ERA-interim reanalysis: Configuration and performance of the data assimilation system.
690 *Quarterly Journal of the Royal Meteorological Society*, 137(656), 553–597. [https://doi.org/](https://doi.org/10.1002/qj.828)
691 [10.1002/qj.828](https://doi.org/10.1002/qj.828)

692

693 Dudhia, J. (1989). Numerical study of convection observed during the winter monsoon
694 experiment using a mesoscale two dimensional model. *J. Atmos. Sci.*, 46, 3077–3107.

695 Emanuel, K.A., David Neelin, J. and Bretherton, C.S. (1994). On large-scale circulations in
696 convecting atmospheres. *Q.J.R. Meteorol. Soc.*, 120: 1111-
697 1143. <https://doi.org/10.1002/qj.49712051902>

698 Friedrich, K., Kalina, E. A., Masters, F. J., & Lopez, C. R. (2013). Drop-Size Distributions in
699 Thunderstorms Measured by Optical Disdrometers during VORTEX2, *Monthly Weather*
700 *Review*, 141(4), 1182-1203

701 Freier, G. (1960), The coalescence of water drops in an electric field, *J. Geophys. Res.*, 65, 3979-
702 3985.
703

704 Giannaros, T. M., Kotroni, V., and Lagouvardos, K. (2015). Predicting lightning activity in
705 Greece with the Weather Research and Forecasting (WRF) model. *Atmospheric Research*,
706 156, 1–13.

707 Goswami B.B., B.N.(Goswami 2016). A Road Map for Improving Dry-Bias in Simulating the
708 South Asian Monsoon Precipitation by Climate Models, *Climate Dynamics*,
709 DOI:10.1007/s00382-016-3439-2

710 Grabowski, W. W. (2015). Untangling microphysical impacts on deep convection applying a
711 novel modeling methodology, *J. Atmos. Sci.*, **72**, 2446– 2464.
712

713 Grabowski, W. W., & Morrison, H. (2020). Do Ultrafine Cloud Condensation Nuclei Invigorate
714 Deep Convection?, *J. Atmos Sci*, 77(7), 2567-2583.
715

716 Hazra, A., B. N. Goswami, and J.-P. Chen (2013). Role of interactions between aerosol radiative
717 effect, dynamics, and cloud microphysics on transitions of monsoon intraseasonal
718 oscillations, *J. Atmos. Sci.*, 70, 2073–2087, doi:10.1175/JAS-D-12-0179.1.
719

720 Hong, S.-Y., and J.-O. J. Lim (2006). The WRF single-moment 6-class microphysics scheme
721 (WSM6), *J. Korean Meteor. Soc.*, 42, 2, 129–151.
722

723 Houze, R. A. (1997). Stratiform precipitation in regions of convection: A meteorological
724 paradox? *Bull. Am. Meteorol. Soc.*, 78(10), 2179–2196.
725

726 Joss, J. & Waldvogel, A. PAGEOPH (1967). 68: 240. doi: 10.1007/BF00874898
727

728 Khain, A., M. Arkhipov, M. Pinsky, Y. Feldman, and Y. Ryabov (2004). Rain enhancement and
729 fog elimination by seeding with charged droplets. Part 1: Theory and numerical simulations,
730 *J. Appl. Meteorol.*, 43, 1513–1529, doi:10.1175/JAM2131.1.
731

732 Konwar, M., S. K. Das, S. M. Deshpande, K. Chakravarty, and B. N. Goswami (2014).
733 Microphysics of clouds and rain over the Western Ghat, *J. Geophys. Res. Atmos.*, 119, doi:
734 10.1002/2014JD021606.

735 Kumjian, M. R., and A. V. Ryzhkov (2010). The impact of evaporation on polarimetric
736 characteristics of rain: Theoretical model and practical implications. *J. Appl. Meteor.*
737 *Climatol.*, 49, 1247–1267.

738 Kumjian, M. R., & Ryzhkov, A. V. (2008). Polarimetric Signatures in Supercell
739 Thunderstorms, *Journal of Applied Meteorology and Climatology*, 47(7), 1940-1961
740

741 Kessler, E (1969). On the Distribution and Continuity of Water Substance in Atmospheric
742 Circulations. *Meteor. Monogr.*, No.32, *Amer. Meteor. Soc.*, 84 pp.
743

744 Kessler, E., (1974). Model of precipitation and vertical air currents. *Tellus*, 26, 519–542.
745

746 Khain, A., Rosenfeld, D., and Pokrovsky, A (2005). Aerosol impact on the dynamics and
747 microphysics of deep convective clouds. *Quarterly Journal of the Royal Meteorological*
748 *Society*, 131(611):2639–2663, ISSN 00359009. doi: 10.1256/qj.04.62.
749

750 Kumar, V. V., C. Jakob, A. Protat, C. R. Williams, and P. T. May (2015). Mass-flux
751 characteristics of tropical cumulus clouds from wind profiler observations at Darwin,
752 Australia, *J. Atmos. Sci.*, 72, 1837– 1855, doi:10.1175/JAS-D-14-0259.1
753

754 Lesins, G. B., , R. List, , and P. I. Joe, (1980). Ice accretions. Part I: Testing of new atmospheric
755 icing concepts. *J. Rech. Atmos.*, **14**, 347–356.

756

757 Lhermitte, R. M., and E. R. Williams (1985). Thunderstorm electrification: A case study, *J.*
758 *Geophys. Res.*, **90**, 6071-6078.

759

760 Liu, C., E. R. Williams, E. J. Zipser, and G. Burns (2010). Diurnal variations of global
761 thunderstorms and electrified shower clouds and their contribution to the global electrical
762 circuit, *J. Atmos. Sci.*, **67**, 309–323, doi:10.1175/2009JAS3248.1.

763

764 Löffler-Mang, M., and J. Joss (2000). An optical disdrometer for measuring size and velocity of
765 hydrometeors, *J. Atmos. Oceanic Technol.*, **17**, 130–139.

766 Low, T. B., and R. List, (1982a) Collision, coalescence, and breakup of raindrops. Part I:
767 Experimentally established coalescence efficiencies and fragment size distributions in
768 breakup. *J. Atmos. Sci.*, **39**, 1591–1606, doi:10.1175/1520-
769 0469(1982)039,1591:CCABOR.2.0.CO;2.

770

771 MacGorman, D. R., & Burgess, D. W. (1994). Positive Cloud-to-Ground Lightning in Tornadic
772 Storms and Hailstorms, *Monthly Weather Review*, **122**(8), 1671-1697

773

774 Mattos, E. V., L. A. T. Machado, E. R. Williams, and R. I. Albrecht (2016). Polarimetric radar
775 characteristics of storms with and without lightning activity, *J. Geophys. Res. Atmos.*,
776 **121**, 14, 201–14, 220, doi:10.1002/2016JD025

777

778 Markowski, P. M., , J. M. Straka, , and E. N. Rasmussen (2003). Tornadogenesis resulting from
779 the transport of circulation by a downdraft: Idealized numerical simulations. *J. Atmos.*
780 *Sci.*, **60**, 795–823.

781

782 Mlawer, E.J., Taubman, S.J., Brown, P.D., Iacono, M.J., Clough, S.A. (1997) Radiative transfer
783 for inhomogeneous atmosphere: RRTM, a validated correlated-k model for the long-wave. *J.*
784 *Geophys. Res.* **102**, 16663–16682. <http://dx.doi.org/10.1029/97JD00237>.

785
786 Morrison, H., G. Thompson, and V. Tatarskii (2009). Impact of cloud microphysics on the
787 development of trailing stratiform precipitation in a simulated squall line: Comparison of
788 one- and two-moment schemes. *Mon. Wea. Rev.*, **137**, 991–1007
789

790 Morrison, H., Tessendorf, S. A., Ikeda, K., and Thompson, G. (2012). Sensitivity of a simulated
791 midlatitude squall line to parameterization of raindrop breakup. *Monthly Weather Review*,
792 **140**, 2437–2460.

793 Mudiar, D., Pawar, S. D., Hazra, A., Konwar, M., Gopalakrishnan, V., Srivastava, M. K., and
794 Goswami, B. N. (2018). Quantification of observed electrical effect on the raindrop size
795 distribution in tropical clouds. *Journal of Geophysical Research: Atmospheres*, **123**.
796 <https://doi.org/10.1029/2017JD028205>

797 Mudiar D., S.D. Pawar, A Hazra, V. Gopalkrishnan, D.M. Lal, K. Chakravarty, M. A.
798 Domkawale, M. K. Srivastava, B.N. Goswami, and E. Williams (2021a), Lightning and
799 precipitation: The possible electrical modification of observed raindrop size distributions,
800 *Atmospheric Research*, Volume 259, 2021, 105663, ISSN 0169-8095,
801 <https://doi.org/10.1016/j.atmosres.2021.105663>.

802 Mudiar, D., Hazra, A., Pawar, S. D., Karumuri, R. K., Konwar, M., Mukherjee, S., et al.
803 (2022). Role of electrical effects in intensifying rainfall rates in the tropics. *Geophysical*
804 *Research Letters*, **49**, e2021GL096276. <https://doi.org/10.1029/2021GL096276>

805 Murugavel, P., Pawar, S.D. and Gopalakrishnan, V. (2014), Climatology of lightning over
806 Indian region and its relationship with convective available potential energy. *Int. J.*
807 *Climatol.*, **34**: 3179-3187. <https://doi.org/10.1002/joc.3901>

808 Mudiar, D., Pawar, S. D., Gopalakrishnan, V., and Williams, E. (2021b). Electric Field
809 Enlarges Raindrops beneath Electrified Clouds: Observational Evidence. *Geophysical*
810 *Research Letters*, **48**, e2021GL093577. <https://doi.org/10.1029/2021GL093577>

811 Nielsen J.K., C. Maus, D. Rzesanke and T. Leisner (2011). Charge-induced stability of water
812 droplets in subsaturated environment, *Atmos. Chem. Phys.*, vol. 11, no. 5, 2031–2037.

813 Ochs, H. T., III, and R. R. Czys (1987). Charge effects on the coalescence of water drops in free
814 fall, *Nature*, 327, 606–608.

815 Pawar S.D., D.M. Lal, P. Murugavel (2012), Lightning characteristics over central India during
816 Indian summer monsoon, *Atmospheric Research*, Volume 106, 44-49,

817 Pawar S.D., V. Gopalakrishnan, P. Murugavel , N.E. Veremey and A. A. Sinkevich (2017).
818 Possible role of aerosols in the charge structure of isolated thunderstorms, *Atmospheric*
819 *Research* 183 463, 331–340.

820 Peters, G., B. Fischer, H. Münster, M. Clemens, and A. Wagner (2005). Profiles of raindrop
821 size distributions by micro rain radars, *J. Appl. Meteorol.*, 44, 1930–1949.

822 Piepgrass, M. V., E. P. Krider, and C. B. Moore, (1982). Lightning and surface rainfall during
823 Florida thunderstorms, *J. Geophys. Res.*, 87, 11, 193- 11, 201.

824 Price, C., and Federmesser, B. (2006), Lightning-rainfall relationships in Mediterranean winter
825 thunderstorms, *Geophys. Res. Lett.*, 33, L07813, doi:[10.1029/2005GL024794](https://doi.org/10.1029/2005GL024794).

826

827 Pruppacher H.R. and J.D. Klett (1996). *Microphysics of Clouds and Precipitation* (second
828 edition), springer.

829 Raut, B. A., Konwar, M., Murugavel, P., Kadge, D., Gurnule, D., Sayyed, I., et al.
830 (2021). Microphysical Origin of Raindrop Size Distributions During Indian
831 Monsoon. *Geophysical Research Letters*, 48,
832 e2021GL093581. <https://doi.org/10.1029/2021GL093581>

833 Reisner, J., R. M. Rasmussen, and R. T. Bruintjes, (1998). Explicit forecasting of supercooled
834 liquid water in winter storms using the MM5 forecast model. *Quart. J. Roy. Meteor. Soc.*,
835 124, 1071– 1107

836 Rasmussen, R. M., , and A. J. Heymsfield, (1987b). Melting and shedding of graupel and hail.
837 Part II: Sensitivity study. *J. Atmos. Sci.*, 44, 2764–2782.

838
839 Rogers R. R. and M. K. Yau (1989). *A Short Course in Cloud Physics* (Third edition).
840
841 Rosenfeld, D (1999). TRMM observed first direct evidence of smoke from forest fires inhibiting
842 rainfall. *Geophysical Research Letters*, 26(20):3105–3108. ISSN 00948276. doi:
843 10.1029/1999GL006066.
844
845 Rosenfeld D, U. Lohmann, G. B. Raga, C. D. O’Dowd, M. Kulmala, S. Fuzzi, A. Reissell, and
846 M. O. Andreae (2008). Flood or drought: How do aerosols affect precipitation? *Science*,
847 321, 1309–1313, doi:10.1126/science.1160606.
848
849 Rutledge, S. A., and P. V. Hobbs (1983). The mesoscale and microscale structure of organization
850 of clouds and precipitation in midlatitude cyclones. VIII: A model for the “seeder-feeder”
851 process in warm-frontal rainbands. *J. Atmos. Sci.*, 40, 1185–1206.
852
853 Ryzhkov, A. V., Kumjian, M. R., Ganson, S. M., & Khain, A. P. (2013). Polarimetric Radar
854 Characteristics of Melting Hail. Part I: Theoretical Simulations Using Spectral
855 Microphysical Modeling, *Journal of Applied Meteorology and Climatology*, 52(12), 2849-
856 2870
857 Schlamp, R. J., S. N. Grover, and H. R. Pruppachcr, (1976). A numerical investigation of the
858 effects of electric charge and vertical external electric fields on the collision efficiency of
859 cloud drops, *J. Atmos. Sci.*, 33, 1747-1755.
860
861 Snook, N., and Xue, M. (2008), Effects of microphysical drop size distribution on
862 tornadogenesis in supercell thunderstorms, *Geophys. Res. Lett.*, 35, L24803,
863 doi:10.1029/2008GL035866.
864 Srivastava, R. C., (1985). A simple model of evaporatively driven downdraft: Application to
865 microburst downdraft. *J. Atmos. Sci.*, 42, 1004–1023.
866

867 Srivastava, R. C. (1987). A model of intense downdrafts driven by the melting and evaporation
868 of precipitation. *J. Atmos. Sci.*, **44** , 1752–1774.
869

870 Steiner, M., , J. A. Smith, , and R. Uijlenhoet (2004). A microphysical interpretation of radar
871 reflectivity–rain-rate relationships. *J. Atmos. Sci.*, **61** , 1114–1131.
872

873 Sun L, Qie XS, Mansell ER et al (2018) Feedback effect of electric field force on electrification
874 and charge structure in thunderstorm. *Acta Phys Sin* 67(16):169201–169201
875

876 Takahashi, T., (1978). Riming electrification as a charge generation mechanism in
877 thunderstorms. *J. Atmos. Sci.*, 35, 1536–1548.
878

879 Takahashi, T. (1984). Thunderstorm electrification- A numerical study, *J. Atmos. Sci.*, 41, 2541-
880 2558.
881

882 Tao, W. K., Chen, J. P., Li, Z., Wang, C., and Zhang, C (2012). Impact of aerosols on convective
883 clouds and precipitation. *Reviews of Geophysics*, 50(2). ISSN 87551209. doi:
884 10.1029/2011RG000369.
885

886 Tao, W.-K., and Li, X. (2016). The relationship between latent heating, vertical velocity, and
887 precipitation processes: The impact of aerosols on precipitation in organized deep
888 convective systems, *J. Geophys. Res. Atmos.*, 121, 6299– 6320, doi:[10.1002/2015JD024267](https://doi.org/10.1002/2015JD024267).
889

890 Tokay, A., & Short, D. A. (1996). Evidence from Tropical Raindrop Spectra of the Origin of
891 Rain from Stratiform versus Convective Clouds, *Journal of Applied Meteorology and*
892 *Climatology*, 35(3), 355-371
893

894 Tyagi, A. (2007), Thunderstorm climatology over Indian region. *Mausam*, 58, 189–212.
895

896 Virts, K. S., and R. A. Houze Jr. (2015). Variation of lightning and convective rain fraction in
897 mesoscale convective systems of the MJO. *J. Atmos. Sci.*, 72, 1932–1944, doi:10.1175/JAS-
898 D-14-0201.1

899

900 Waldvogel, A. (1974). The N0 Jump of Raindrop Spectra, *Journal of Atmospheric*
901 *Sciences*, 31(4), 1067-1078.

902

903 Williams, E. R., and R. M. Lhermitte (1983). Radar tests of the precipitation hypothesis for
904 thunderstorm electrification, *J. Geophys. Res.*, 88, 10,984-10,992.

905

906 Williams, E. R., S. A. Rutledge, S. C. Geotis, N. Renno, E. Rasmussen, and T. Rickenbach
907 (1992). A radar and electrical study of tropical hot towers, *J. Atmos. Sci.*, 49, 1386–1395.

908

909 Williams, E. R., & Renno, N. O. (1993). An analysis of the conditional instability of the tropical
910 atmosphere. *Monthly Weather Review*, **121**(1), 21– 36. [https://doi.org/10.1175/1520-](https://doi.org/10.1175/1520-0493(1993)121<0021:AAOTCI>2.0.CO;2)
911 [0493\(1993\)121<0021:AAOTCI>2.0.CO;2](https://doi.org/10.1175/1520-0493(1993)121<0021:AAOTCI>2.0.CO;2)

912

913 Williams, E. R. (2005). Lightning and climate: A review, *Atmos. Res.*, 76, 272–287.

914

915 Williams E.R. (2001). The Electrification of Severe Storms. In: Doswell C.A. (eds) Severe
916 Convective Storms. *Meteorological Monographs. American Meteorological Society*,
917 Boston, MA. https://doi.org/10.1007/978-1-935704-06-5_13.

918

919 Williams, E. R., and Co-authors (2010). Ground-based detection of sprites and their parent
920 lightning flashes over Africa during the 2006 AMMA campaign. *Quart. J. Roy. Meteor.*
921 *Soc.*, **136**, 257–271, doi:<https://doi.org/10.1002/qj.489>.

922

923 Winn, W. P., G. W. Schwede, and C. B. Moore (1974). Measurements of electric fields in
924 thunderclouds, *J. Geophys. Res.*, 79, 1761– 1767.

925 Zhang, G., Xue, M., Cao, Q., & Dawson, D. (2008). Diagnosing the Intercept Parameter for
926 Exponential Raindrop Size Distribution Based on Video Disdrometer Observations: Model
927 Development, *Journal of Applied Meteorology and Climatology*, 47(11), 2983-2992

928
929 Zhang, G., J. Sun, and E. A. Brandes (2008). Improving parameterization of rain microphysics
930 with disdrometer and radar observations. *J. Atmos. Sci.*, **63**, 1273–1290.

931 Zhang, H., Zhang, Y., He, H., Xie, Y., & Zeng, Q. (2017). Comparison of Raindrop Size
932 Distributions in a Midlatitude Continental Squall Line during Different Stages as Measured
933 by Parsivel over East China, *Journal of Applied Meteorology and Climatology*, 56(7), 2097-
934 2111

935

936

937

938

939

940 **Figure Captions**

941 **Figure 1:** (a) Depiction of topographical map of the High Altitude Cloud Physics Laboratory
942 (HACPL), Mahabaleshwar, (India; 17.92 N, 73.66 E) and Atmospheric Electricity Observatory
943 (AEO) at Pune, (India; 18.53N, 73.80E). (b) Nested model domain.

944 **Figure 2:** (a-b) Height Time Index (HTI) of radar reflectivity factor (dBZ) for the rain events
945 observed over the High Altitude Cloud Physics Laboratory (HACPL), Mahabaleshwar on
946 13May, 2015 (SE) and 04 October, 2014 (WE) respectively. The presence of melting layer can
947 be observed at mean sea level (msl) height of 4.6 km. (c-d) surface rain rates (mm hr^{-1})
948 measured by JW disdrometer. (e-f) Mass weighted diameter (MWD) of raindrops measured
949 (mm) by JW disdrometer. (g-h) Rain intercept parameter, N_0 derived from JW disdrometer using
950 methods of moments following Konwar et al., (2014).

951 **Figure 3:** Scatter plot of total lightning (intracloud+cloud-to-ground) observed by the
952 Maharashtra lightning location network (MLLN) on 13 May 2015 near the HACPL.

953 **Figure 4:** (a) Scatter plot of N_0 ($\text{m}^{-3} \text{mm}^{-1}$) vs. rainwater content W (gm m^{-3}) for strongly
954 electrified (SE) events (indicated by blue stars) observed at the High Altitude Cloud Physics
955 Laboratory (HACPL). The values of N_0 and W are calculated from JW disdrometer
956 measurements using moments method following Konwar et al., (2014). The red line is the best-
957 fit line using the least squares method. The superimposed red dots correspond to the events on 13

958 May, 2015 (SE) and the black dots correspond to the events on 04 October, 2014 (WE). (b) Bar
959 plot representation of values of N_0 for some SE and WE events observed at the HACPL. The x
960 coordinate indicates number of storms.

961 **Figure 5:** Rain evaporation rate ($\text{kg kg}^{-1} \text{s}^{-1}$) for the events shown in Figure 2(a-b). The
962 evaporation rate is calculated by using equation (1) from the microrain radar (MRR) measured
963 values of raindrop size distribution parameters. The vertical resolution of MRR measurement is
964 300m. SE and WE indicate strongly and weakly electrified events, respectively. The height is
965 measured from mean sea level (msl). The msl height of the HACPL is 1.3 km. Data from the
966 lowest measuring height (1.6km) is discarded.

967 **Figure 6:** Bar graph representation of N_0 ($\text{m}^{-3} \text{mm}^{-1}$) vs. surface-measured E field (V m^{-1}) for a
968 few SE events observed for the year 2008 at the Atmospheric Electricity Observatory (AEO) at
969 Pune (a)3rd June, (b) 31 August,(c) 8 September and (d) 9 September. The values of N_0 are
970 grouped in E field bins of width 500V m^{-1} . Each bar in the plots corresponds to the mean value
971 of the respective bin. (e-h) The corresponding bar graph representation of rain evaporation rates
972 (ER) vs. E field for the same events as shown in (a-d).

973 **Figure 7:** Results from the idealized simulations (a) accumulated rain (mm) (b) Evaporation rate
974 ($\text{kg kg}^{-1} \text{s}^{-1}$) (c) Maximum vertical velocity (ms^{-1}). The blue curves correspond to the default
975 wsm6 scheme and the green curves correspond to the modified scheme indicated as wsm6(M).

976 **Figure 8:** Results from observed case (13 May 2015) simulation (a) Comparison of simulated
977 rain rate to the observed rain rate at the HACPL (mm hr^{-1}). (b) Daily accumulated rain (mm),
978 averaged over a $25\text{km} \times 25\text{km}$ box, with the HACPL being in the middle. IMD indicates Indian
979 Meteorological Department, TRMM indicates the Tropical Rainfall Measuring Mission and
980 JWD indicates JW disdrometer measurements.

981 **Figure 9:** Results from observed case simulation (13 May 2015). (a) Height Time Index (HTI) of
982 area-averaged vertical velocity (m s^{-1}) for wsm6 (b) same as (a) but for wsm6(M).

983 **Figure 10:** Results from observed case simulation (5 May 2015). (a) Height Time Index (HTI) of
984 area-averaged vertical velocity (m s^{-1}) for wsm6 (b) same as (a) but for wsm6(M).

985 **Figure 11:** Schematic representation of the evolution of weakly and strongly electrified storms.
986 In a weakly electrified (WE) storm, the number of smaller raindrops are numerous, the
987 evaporation of which resulted in latent cooling, thereby initiating the downdraft at the mature
988 stage of the storm. In strongly electrified (SE) storms, electrically induced coalescence reduces
989 the number of smaller raindrops and increases the number of larger ones and thereby reducing
990 the latent cooling. The reduction of latent cooling delays the initiation of downdraft. This process
991 acts to provide positive feedback to storm updraft intensity in strongly electrified storms. The
992 length of the arrows indicates the strength of vertical velocity.

993

994 **Table 1:** Results from the two observed strongly electrified (SE) events simulations.

995

Events	Observed cloud parameters	Control run ($N_0 = 8 \times 10^6 m^{-4}$) wsm6	Modified run ($N_0 = 1.6 \times 10^6 m^{-4}$) wsm6(M)	Relative changes
13May, 2015	CTH =8.5km FR =4flashes min^{-1} RI = 4.33 mm hr^{-1} R =11.32 mm T= 2 hours	R =6.77 mm, Wmax = 34.70 ms^{-1} QI = 3.87×10^{-4} kg kg^{-1}	R = 8.233 mm, Wmax = 37.44 ms^{-1} QI = 4.21×10^{-4} kg kg^{-1}	% change in R=21%
5 May, 2015	CTH =not available FR =9 flashes min^{-1} RI = 16.42 mm hr^{-1} R =11.52 mm T=2 hours	R = 2.94mm, Wmax =48.01 ms^{-1} QI = 2.49×10^{-4} kg kg^{-1}	R = 5.18 mm , Wmax = 51.52 ms^{-1} , QI = 3.14×10^{-4} kg kg^{-1}	% change in R=76%

996

997 Note: ‘R’ indicates area-averaged accumulated rain rate in mm. The observed R values are
998 obtained from the Tropical Rain Measuring Mission (TRMM) 3B-42 precipitation datasets. FR
999 indicates flash rate obtained from Maharashtra Lightning Location Network (MLLN). ‘CTH’
1000 indicates cloud top height obtained from the Moderate Resolution Imaging Spectroradiometer
1001 (MODIS) (Terra platform) collection 6. ‘RI’ indicates peak rain intensity, ‘T’ indicates storm life
1002 time, ‘ N_0 ’ is the rain intercept parameter, ‘QI’ indicate domain-averaged total mass mixing ratio
1003 of ice-phase hydrometeors (graupel+ice+snow) and ‘Wmax’ is the maximum simulated vertical
1004 velocity.

1005

1006

1007

1008

1009

1010

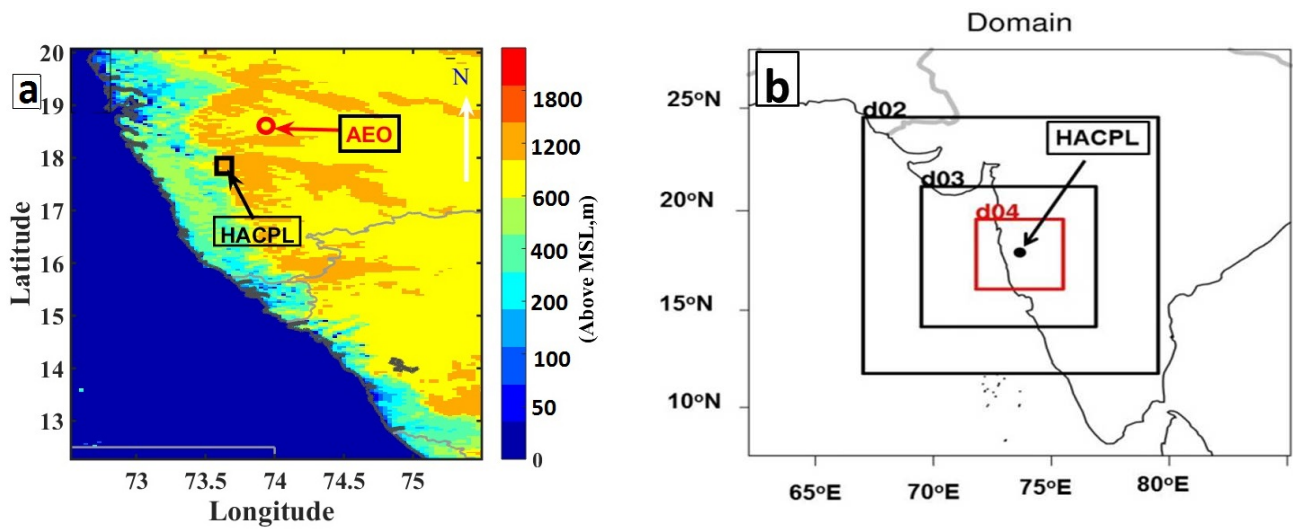


Figure 1: (a) topographical map depicting the High Altitude Cloud Physics Laboratory (HACPL), Mahabaleshwar, (India; 17.92 N, 73.66 E) and Atmospheric Electricity Observatory (AEO) at Pune, (India; 18.53N, 73.80E). (b) Nested model domain

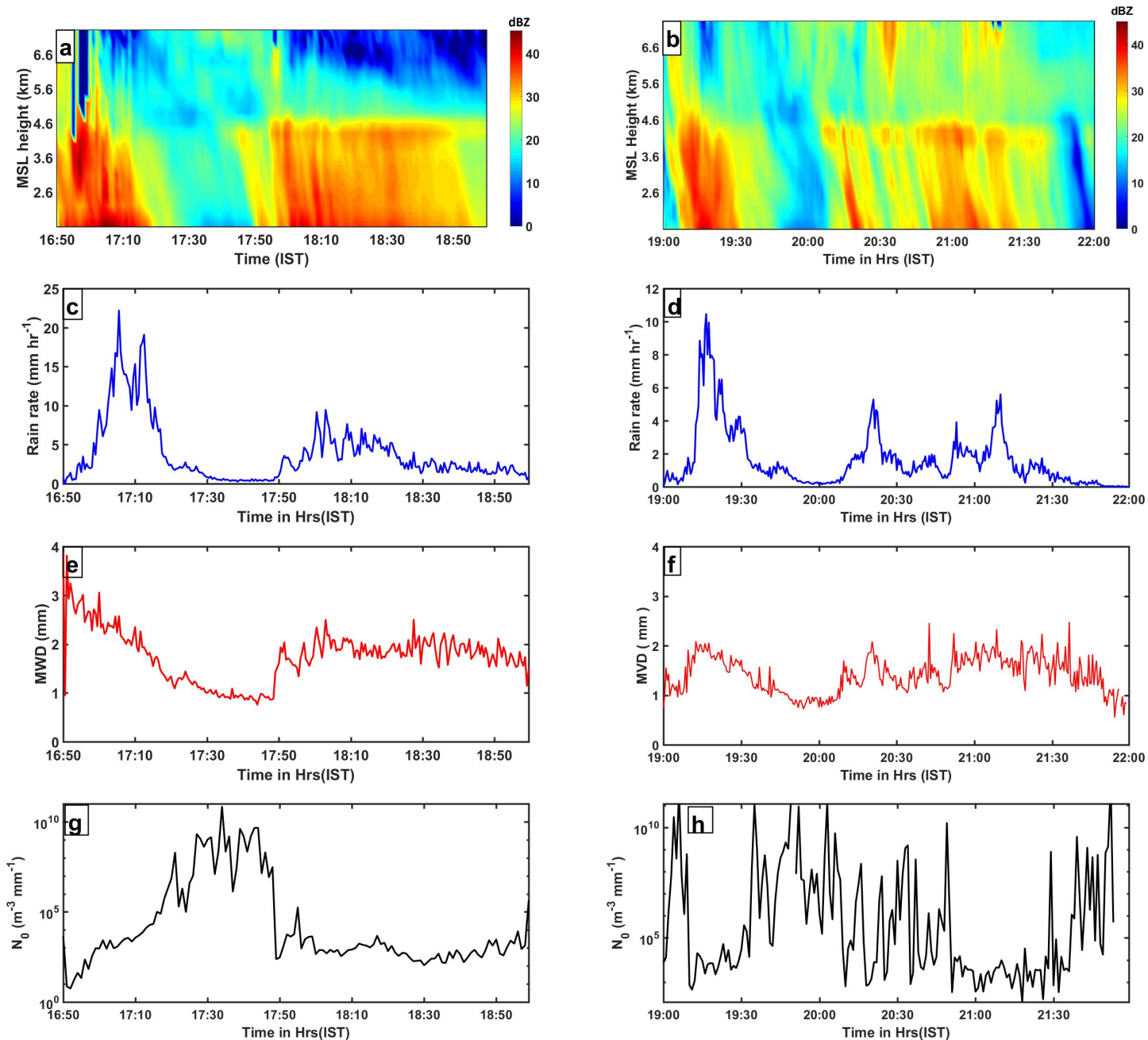


Figure 2: (a-b) Height Time Index (HTI) of radar reactivity factor (dbz) for the rain events observed over the High Altitude Cloud Physics Laboratory (HACPL), Mahabaleshwar on 13 May, 2015 (SE) and 04 October, 2014 (WE) respectively. The presence of melting layer can be observed at msl height of 4.6 km. (c-d) surface rain rates (mm hr⁻¹) measured by JW disdrometer, (e-f) Mass weighted diameter (MWD) of raindrops measured (mm) by JW disdrometer. (g-h) Intercept parameter N_{0r} derived from JW disdrometer using moments methods following Konwar et al., (2014).

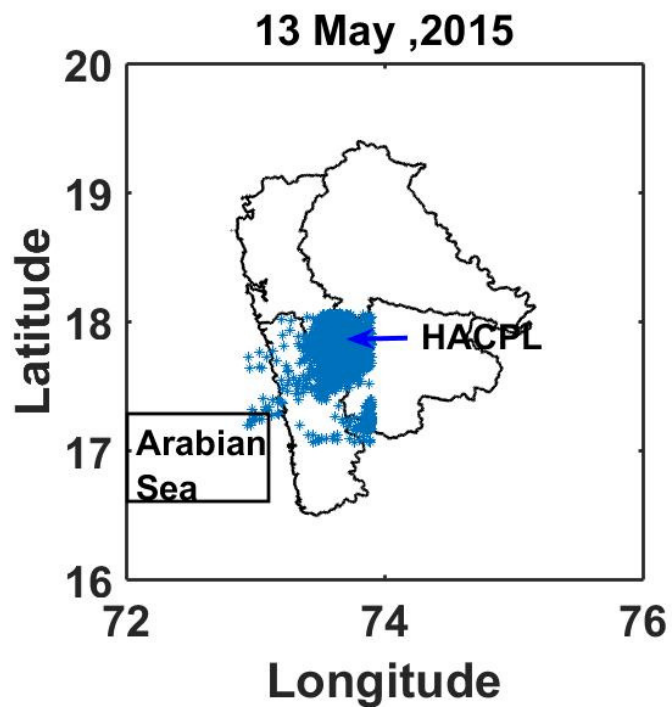


Figure 3: Scatter plot of lightning observed by the Maharashtra lighting location network (MLLN) on 13 May, 2015 near the HACPL.

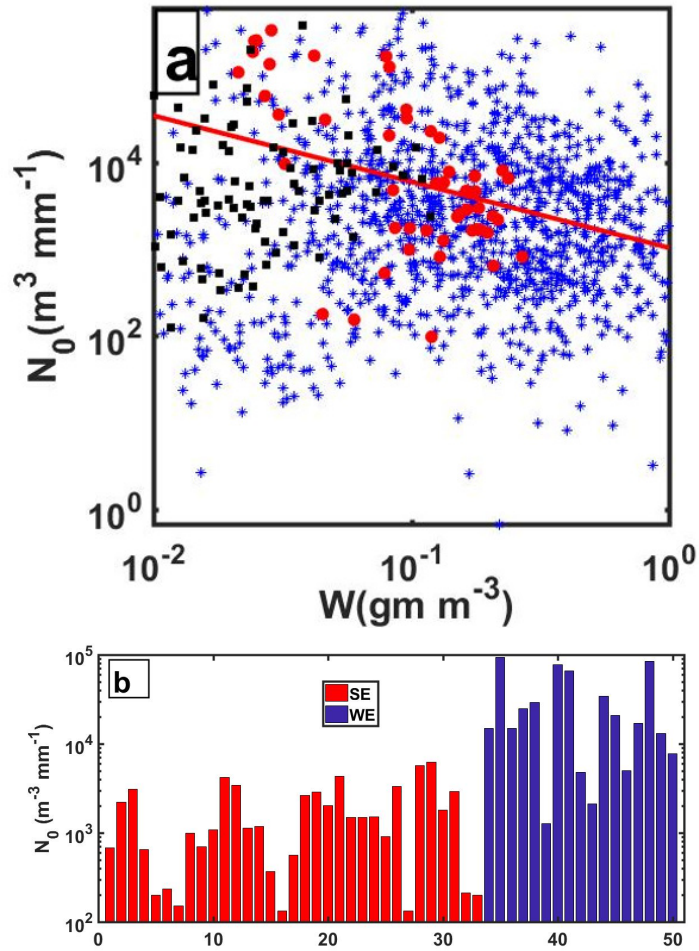


Figure 4: (a) Scatter plot of $N_{0r}(m^{-3}mm^{-1})$ vs rainwater content W ($gm m^{-3}$) for SE events observed at the High Altitude Cloud Physics Laboratory (HACPL). The values of N_{0r} and W are calculated from JW disrometer measurements using moments method following Konwar et al., (2014). The red line is the best-fit line using the least squares method. The superimposed red dots corresponds to the events on 13 May, 2015 (SE) and the black dots corresponds to the events on 03 October, 2014 (WE). (b) Bar plot representation of values of N_{0r} for some SE and WE events observed at the HACPL. The

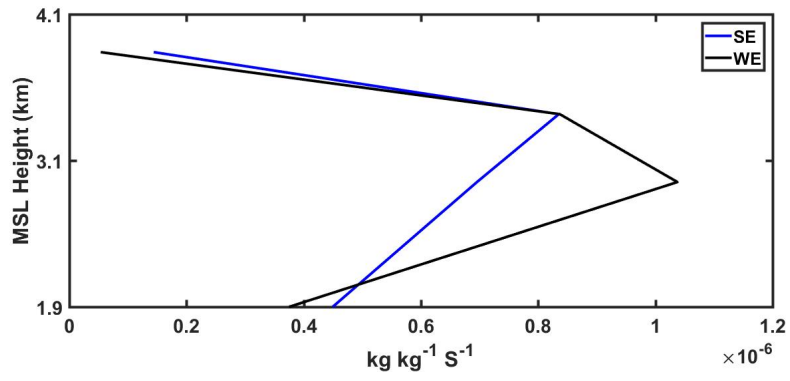


Figure 5: Rain evaporation rate ($\text{kg kg}^{-1} \text{s}^{-1}$) for the events shown in Figure 2(a-b). The evaporation rate is calculated by using equation (1) from the microrain radar (MRR) measured values of raindrop size distribution parameters. SE and WE indicate strongly and weakly electrified.

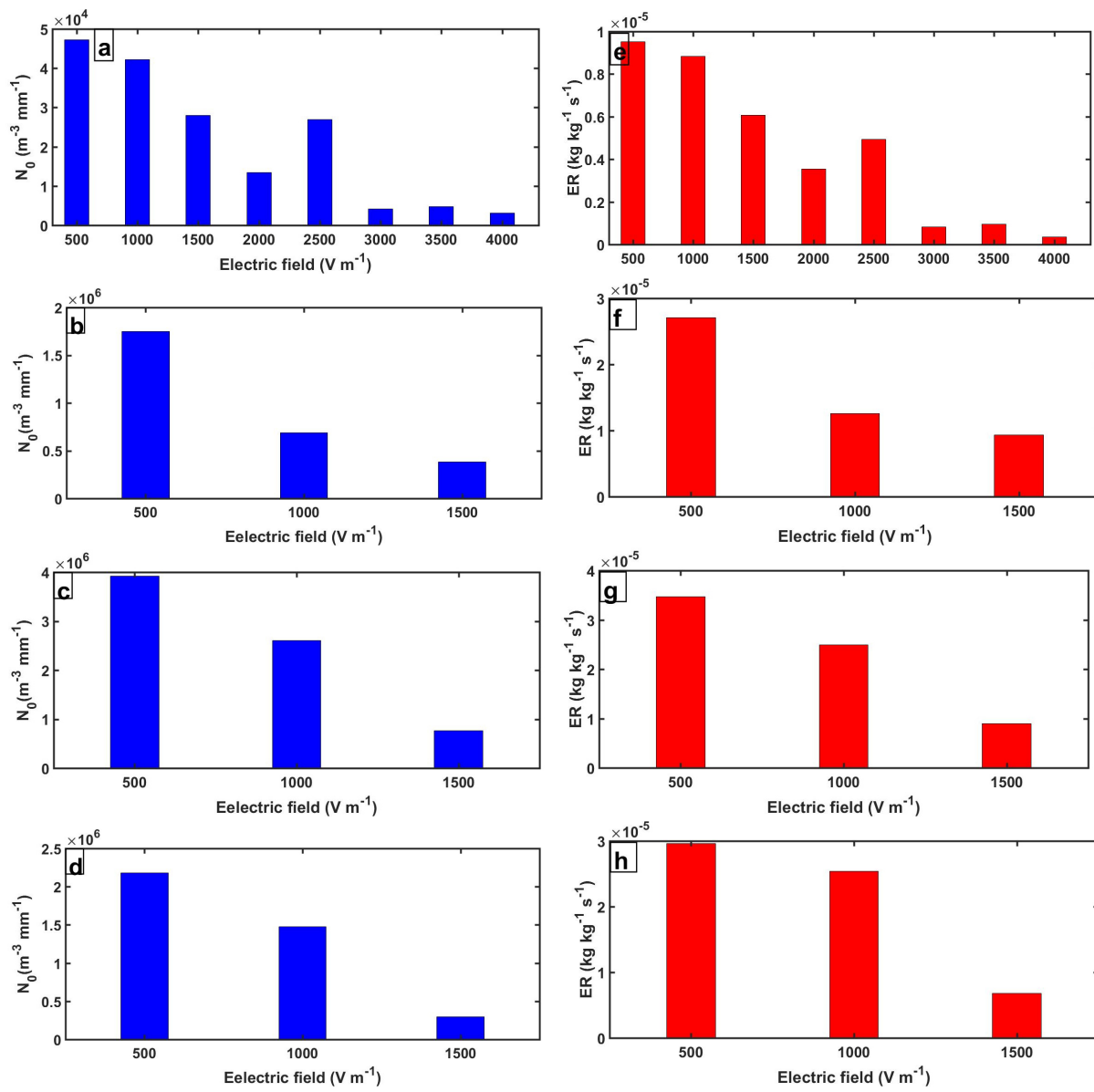


Figure 6: Bar plot of rain intercept parameter, N_0 ($\text{m}^{-3} \text{mm}^{-1}$) vs. surface measured E field (V m^{-1}) for a few SE events observed for the year 2008 at the Atmospheric Electricity Observatory (AEO) at Pune (a) 3rd June, (b) 31 August, (c) 8 September and (d) 9 September. The values of N_0 are grouped in E field bin of width 500 V m^{-1} . (e-h) The corresponding bar plot of evaporation rate (ER) vs. E field for the same events as shown in (a-d).

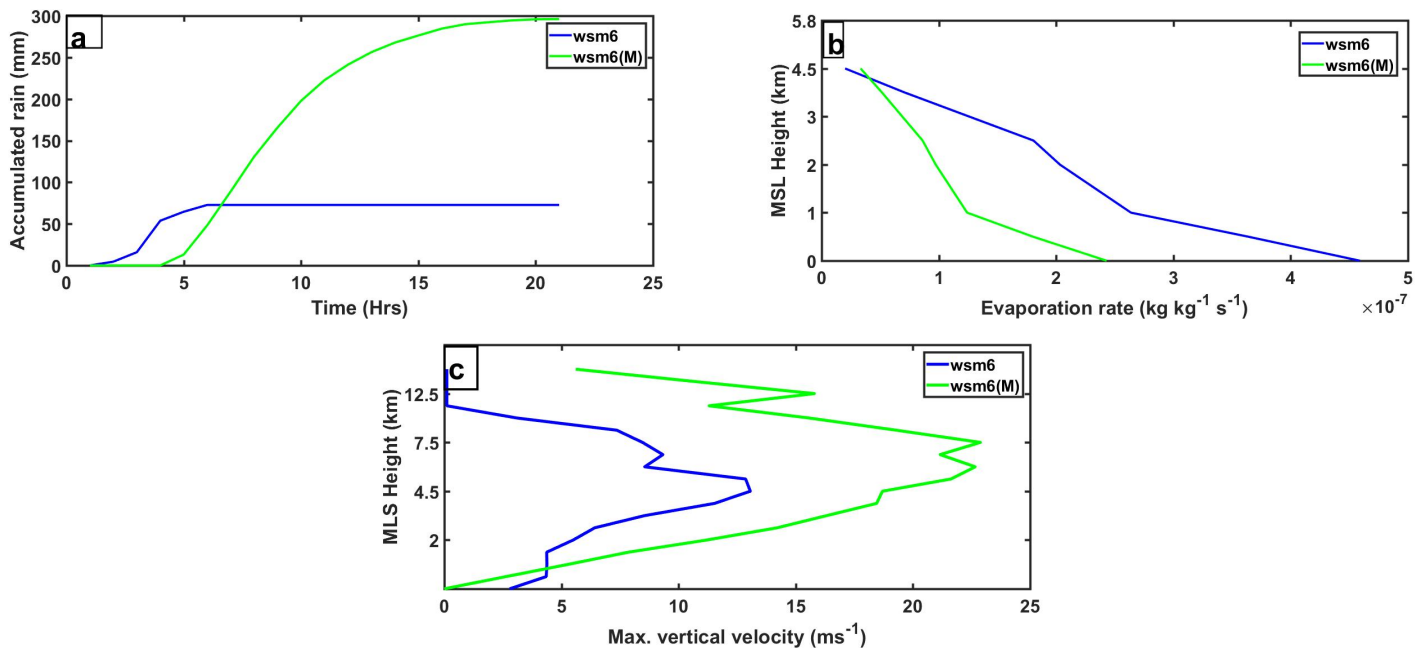


Figure 7: Results from the idealized simulations (a) accumulated rain (mm) (b) Evaporation rate ($\text{kg kg}^{-1} \text{s}^{-1}$) (c) Maximum vertical velocity (m s^{-1}). (d) Vertical profiles of ice phase hydrometeors (kg kg^{-1}). The solid curves correspond to wsm6 scheme and dashed curves correspond to wsm6(M).

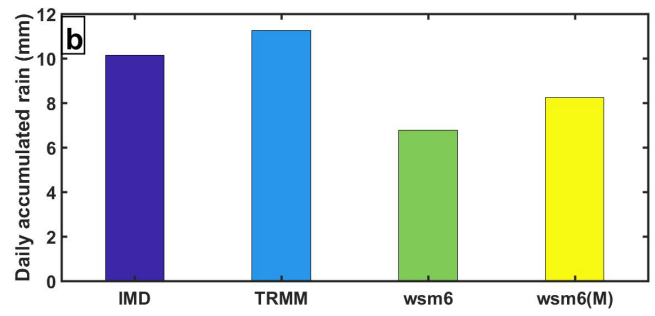
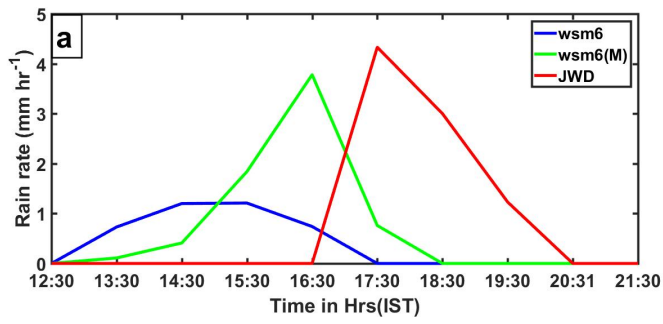


Figure 8: Results from real case (13 May ,2015) simulation (a) Rain rate (mm hr⁻¹).(b) Daily accumulated rain. IMD indicate Indian meteorological department. TRMM indicate the Tropical Rainfall Measuring Mission. (c) Probability Density Function (PDF) for rain .

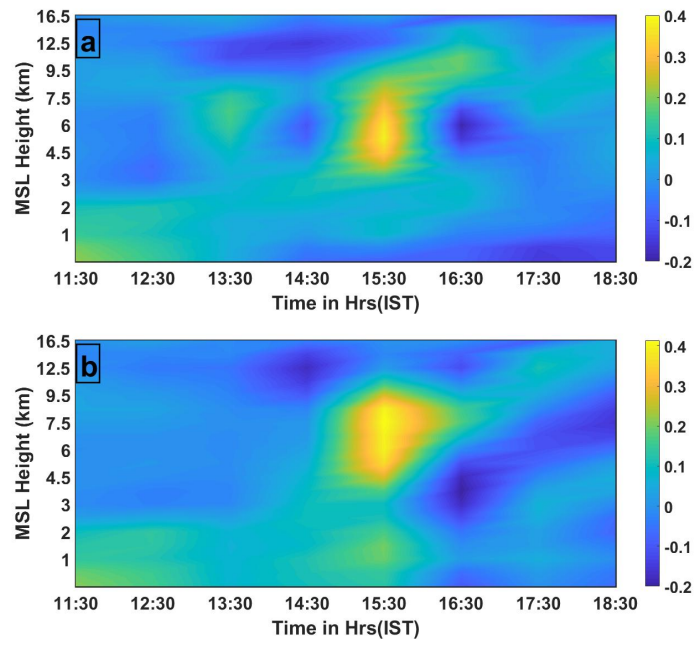


Figure 9: Results from real case simulation (13 May 2015)(a) Height Time Index of area averaged vertical velocity (m s^{-1}) for wsm6 (b) same as (a) but for wsm6(M)

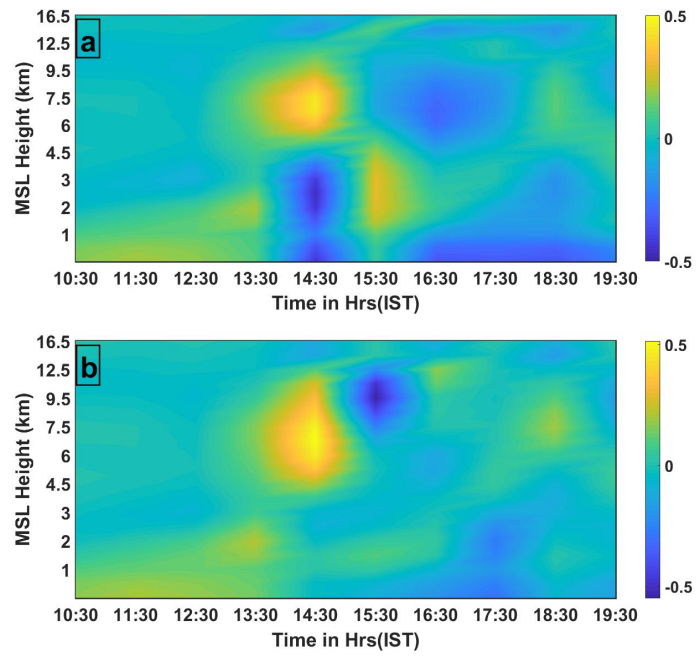


Figure 10: (a) Simulated CAPE for the storm on 13 May, 2015 averaged over a 25km×25km box, the HACPL being in the middle. (b) Total flash count in the said box derived from Maharashtra lightning location network (MLLN) for the storm.

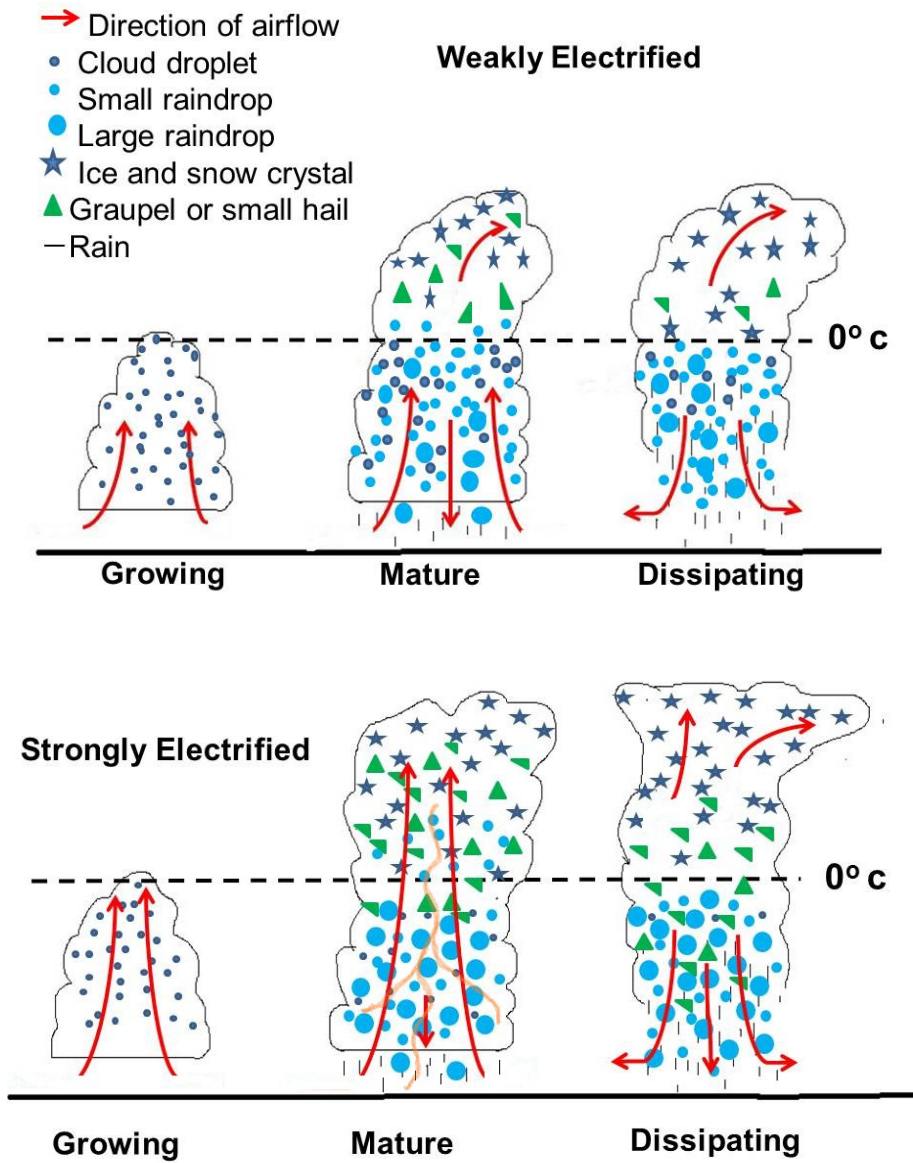


Figure 11: Evolution of weakly and strongly electrified storms. In a weakly electrified storms, number of smaller raindrops are numerous evaporation of which resulted in latent cooling, thereby initiating downdraft at the mature stage of the storm. In strongly electrified storms, electrically induced coalescence reduces the number of smaller raindrops and increase the number of larger ones and thereby reduces the latent cooling. This delays the initiation of downdraft. This process acts to provide a positive feedback to storm updraft intensity in strongly electrified storms. The length of the arrows indicate strenght of vertical velocity.